

COMPUTATIONAL MODELING OF HARDENING CONCRETE AT
MESOSCALE

A THESIS SUBMITTED TO
THE GRADUATE SCHOOL OF NATURAL AND APPLIED SCIENCES
OF
MIDDLE EAST TECHNICAL UNIVERSITY

BY

ÇAĞLAR YILMAZ

IN PARTIAL FULFILLMENT OF THE REQUIREMENTS
FOR
THE DEGREE OF MASTER OF SCIENCE
IN
CIVIL ENGINEERING

APRIL 2023

Approval of the thesis:

**COMPUTATIONAL MODELING OF HARDENING CONCRETE AT
MESOSCALE**

submitted by **ÇAĞLAR YILMAZ** in partial fulfillment of the requirements for the degree of **Master of Science in Civil Engineering Department, Middle East Technical University** by,

Prof. Dr. Halil Kalıpçılar
Dean, Graduate School of **Natural and Applied Sciences**

Prof. Dr. Erdem Canbay
Head of Department, **Civil Engineering**

Assoc. Prof. Dr. Serdar Göktepe
Supervisor, **Civil Engineering, METU**

Examining Committee Members:

Prof. Dr. Sinan Turhan Erdoğan
Civil Engineering, METU

Assoc. Prof. Dr. Serdar Göktepe
Civil Engineering, METU

Assoc. Prof. Dr. Ercan Gürses
Aerospace Engineering, METU

Assist. Prof. Dr. Feyza Soysal Albostan
Civil Engineering, Çankaya University

Assist. Prof. Dr. Halit Cenan Mertol
Civil Engineering, Atılım University

Date:27.04.2023

I hereby declare that all information in this document has been obtained and presented in accordance with academic rules and ethical conduct. I also declare that, as required by these rules and conduct, I have fully cited and referenced all material and results that are not original to this work.

Name, Surname: Çağlar Yılmaz

Signature :

ABSTRACT

COMPUTATIONAL MODELING OF HARDENING CONCRETE AT MESOSCALE

Yılmaz, Çağlar

M.S., Department of Civil Engineering

Supervisor: Assoc. Prof. Dr. Serdar Göktepe

April 2023, 72 pages

Concrete can be conceived as a composite material made up of cement, fine and coarse aggregates, water, and admixtures. The strength gain mechanism of concrete is based on the exothermic chemical reactions between the cement and free water that are collectively referred to as hydration. Generally hydration is accompanied by various physico-chemical phenomena such as the evolution of temperature and water content, thermal and shrinkage-induced volumetric deformations. During the chemical aging of concrete residual stresses develop in the material, especially at the interface between the mortar and coarse aggregates. These residual stresses mainly arise from the constraining effect of aggregates due to their higher stiffness on the mortar. This work is concerned with the computational modeling of hardening concrete at the mesoscale to investigate the effect of the area fraction, segregation, aspect ratio, and the roundness of aggregates under the action of different magnitudes of shrinkage deformations in mortar on the magnitude of residual stresses. For this purpose, a virtual tool for generating the meso-structure of concrete is developed. The generated models at mesoscale are then analyzed numerically to calculate the evolution of principal residual stresses during early ages of samples. The hardened samples incorporating

shrinkage-induced residual stresses are then analyzed under tension to examine the effect of the residual stresses on the tensile strength of concrete at mesoscale using the phase-field fracture method.

Keywords: Constitutive equations, Hardening concrete, Mesoscale, Shrinkage, Phase-Field Method

ÖZ

SERTLEŞEN BETONUN MEZO ÖLÇEKTE HESAPLAMALI MODELLENMESİ

Yılmaz, Çağlar

Yüksek Lisans, İnşaat Mühendisliği Bölümü

Tez Yöneticisi: Doç. Dr. Serdar Göktepe

Nisan 2023 , 72 sayfa

Kompozit bir malzeme olarak da düşünülebilecek beton, çimento, ince ve iri agregalar, su ve katkı malzemelerinin bileşiminden oluşur. Betonun dayanımını kazanması çimento ile su arasında, topluca hidrasyon olarak anılan, ısıveren kimyasal tepkimeler sonucunda olmaktadır. Hidrasyon genellikle, sıcaklık değişimi, su miktarındaki değişim ve bunların sonucunda ortaya çıkan hacimsel şekil değişimleri gibi farklı fiziko-kimyasal olaylarca eşlik edilmektedir. Betonun kimyasal olgunlaşması sırasında, özellikle harç ve agregalar arasında artık gerilmeler oluşmaktadır. Bunlar agregaların harca göre daha rijit olmasından kaynaklanan şekil değiştirme üzerindeki sınırlayıcı etkileri nedeni ile ortaya çıkmaktadır. Bu çalışma, agregaların alan oranı, ayrılma, en-boy oranı ve yuvaklılığının, harçtaki farklı büzülme mertebeleri altında oluşan artık gerilmeler üzerine etkisini incelemek için sertleşen betonun mezo ölçekte hesaplamalı modellenmesini konu almaktadır. Bu amaçla, betonun mezo yapısının oluşturmak için sanal bir araç geliştirilmiştir. Betonun erken yaşlarda oluşan asal artık gerilmelerin hesaplanması için mezo ölçekteki modellerin sayısal olarak analizi gerçekleştirilmiştir. Bu aşama sonrasında büzülme nedeni ile oluşan artık ge-

riilmeleri barındıran sertleşmiş beton numunelerin çekme altında analizleri yapılarak farklı mezo yapılarda oluşan artık gerilmelerin mezo ölçekteki betonun çekme dayanımı üzerine etkisi Faz Alanı Yöntemi ile incelenmiştir.

Anahtar Kelimeler: Bünye denklemleri, Sertleşen beton, Mezo Ölçek, Büzülme, Faz Alanı Yöntemi

ACKNOWLEDGMENTS

First and foremost, I would like to express my deepest gratitude to my supervisor Assoc. Prof. Dr. Serdar Göktepe for his unwavering support and guidance throughout my study. His enthusiasm and curiosity for research are the primary sources of my motivation and encouragement.

I am thankful for the valuable feedback and the time they spent reviewing my thesis to jury members, Prof. Dr. Sinan Turhan Erdoğan, Assoc. Prof. Dr. Ercan Gürses, Assist. Prof. Dr. Feyza Soysal Albostan, and Assist. Prof. Dr. Halit Cenan Mertol.

I would like to thank my family, Zehra Yılmaz, İrfan Yılmaz, and Çağrı Yılmaz for their continuous support throughout my life and unconditional love.

I would like to offer my special thanks to Deniz Ünal for his genuine friendship and support throughout the years.

I am truly grateful to Barış Yıldırım, Berfin Bölükemini, Deniz Naz Kadim, Denizcan Tekin, Eren Yıldırım, Hakan Şenyurt, and Hande Ekin Şahin for their presence and friendship.

TABLE OF CONTENTS

ABSTRACT	v
ÖZ	vii
ACKNOWLEDGMENTS	x
TABLE OF CONTENTS	xi
LIST OF TABLES	xiv
LIST OF FIGURES	xv
LIST OF SYMBOLS	xix
CHAPTERS	
1 INTRODUCTION	1
1.1 Hydration of Concrete	1
1.2 Shrinkage of Concrete	4
1.3 Meso-Structure and Concrete	6
1.4 Scope and Aim of the Thesis	9
1.5 Outline of the Thesis	9
2 GENERATION OF RANDOM MESO-STRUCTURES	11
2.1 Generation of Polygonal Aggregate Particles	11
2.1.1 Grading of Aggregate	13
2.2 Take-and-Place Method	14

2.2.1	Take-Process	14
2.2.2	Place-Process	15
2.3	Generated Structures	17
3	GOVERNING AND CONSTITUTIVE EQUATIONS	19
3.1	Kinematics and State Variables	20
3.2	Governing Equations	22
3.3	Stress Response	24
3.4	Crack Driving Force	25
3.5	Hydration of Cement	26
3.6	Aging Mechanism	27
4	NUMERICAL EXAMPLES	29
4.1	Validations	34
4.1.1	Hardening of Mortar	34
4.1.1.1	Analytical Solution	34
4.1.2	Mesh Convergence	36
4.1.2.1	Hardened Specimen	36
4.1.2.2	Hardening Specimen	37
4.1.3	Statistical Study	38
4.2	Shrinkage-Induced Residual Stress Evolution	42
4.2.1	Area Ratio	43
4.2.2	Segregation	46
4.2.3	Elongation Ratio	48
4.2.4	Shape	49

4.3	Fracture Behavior in Tension	51
4.3.1	Effect of Residual Stresses	54
4.3.2	Comparison of Cases	59
5	CONCLUDING REMARKS	63
	REFERENCES	67

LIST OF TABLES

TABLES

Table 2.1	Steps of Take-Process and Place-Process	16
Table 4.1	Maximum principal stresses ($\text{MPa} \times 10^{-2}$)	31
Table 4.2	Material Parameters	31
Table 4.3	Parameters governing the hydration of mortar	32
Table 4.4	Numerical example cases	33
Table 4.5	Displacement values ($\text{mm} \times 10^{-4}$) in y direction of nodes at left and right upper edge	37
Table 4.6	Cohesive Zone Element Parameters	54

LIST OF FIGURES

FIGURES

Figure 1.1	Autogenous shrinkage findings of Bentz et al. [1] with and without Shrinkage Reducing Admixture	5
Figure 1.2	Autogenous shrinkage findings of Bentz et al. [2] with fine and coarse aggregates	5
Figure 1.3	Autogenous shrinkage findings of Loukili et al. [3]	6
Figure 1.4	Autogenous shrinkage findings of Lu et al. [4] for w/c ratio of 0.3 and 0.4 for different percentage of sand	6
Figure 2.1	An aggregate with its polar coordinates and angles	12
Figure 2.2	The grading curve	17
Figure 2.3	Stages of aggregate placement. The colors of aggregates indicate the corresponding grading interval in Figure 2.2	17
Figure 2.4	Random meso-structures generated	18
Figure 3.1	Sharp crack embedded in a solid body	21
Figure 3.2	Phase-field approximations with different length scale values	22
Figure 4.1	(a) Evolution of degree of hydration (b) Evolution of degree of aging	30
Figure 4.2	The degree of hydration with respect to time	31

Figure 4.3	Applied Shrinkage Strains	32
Figure 4.4	Analytical and numerical results	35
Figure 4.5	Reaction loads with respect to total degrees of freedom	36
Figure 4.6	Displacement in y direction of upper leftmost node with respect to total degrees of freedom	38
Figure 4.7	Nine examples of subcases obtained with control parameters . . .	39
Figure 4.8	Load-displacement at $y = 150$ mm in y direction	40
Figure 4.9	Maximum principal stress of each subcase and its deviation from the average value	40
Figure 4.10	Stiffness values of each subcase and its deviation from the aver- age value	41
Figure 4.11	Density and probability density distribution functions of princi- pal stresses	42
Figure 4.12	Density and probability density distribution functions of stiff- ness values	42
Figure 4.13	Boundary Conditions	43
Figure 4.14	Maximum principal stress values (a) Contour plots (b) Histograms	44
Figure 4.15	β values (a) Contour plots (b) Histograms	45
Figure 4.16	Maximum principal stress values (a) Contour plots (b) Histograms	46
Figure 4.17	β values (a) Contour plots (b) Histograms	47
Figure 4.18	Maximum principal stress values (a) Contour plots (b) Histograms	48
Figure 4.19	β values (a) Contour plots (b) Histograms	49
Figure 4.20	Maximum principal stress values (a) Contour plots (b) Histograms	50
Figure 4.21	β values (a) Contour plots (b) Histograms	51

Figure 4.22	Boundary Conditions	52
Figure 4.23	Unloading reloading path for cohesive zone element	53
Figure 4.24	Control case: (a) Load displacement curve (b) Fracture formation with residual stresses (c) Fracture formation without residual stresses	55
Figure 4.25	Case II: (a) Load displacement curve (b) Fracture formation with residual stresses (c) Fracture formation without residual stresses	55
Figure 4.26	Case III: (a) Load displacement curve (b) Fracture formation with residual stresses (c) Fracture formation without residual stresses	56
Figure 4.27	Case IV: (a) Load displacement curve (b) Fracture formation with residual stresses (c) Fracture formation without residual stresses	57
Figure 4.28	Case V: (a) Load displacement curve (b) Fracture formation with residual stresses (c) Fracture formation without residual stresses	57
Figure 4.29	Case VI: (a) Load displacement curve (b) Fracture formation with residual stresses (c) Fracture formation without residual stresses	58
Figure 4.30	Case VII: (a) Load displacement curve (b) Fracture formation with residual stresses (c) Fracture formation without residual stresses	59
Figure 4.31	Load displacement curve for area ratio comparison	60
Figure 4.32	Load displacement curve for segregation comparison	60
Figure 4.33	Load displacement curve for elongation ratio comparison	61
Figure 4.34	Load displacement curve for shape comparison	62

LIST OF SYMBOLS

$A_{agg}[d_s, d_{s+1}]$	Total area of the segment between d_s and d_{s+1}
A_{c1} , and A_{c2}	Material parameters related with hydration
A_{con}	Area of the cross section
\tilde{A}_ξ	Normalized affinity
A_χ , and A_χ	Model parameters related with aging
d	Crack phase field
d	Opening diameter
d_{max}	Maximum opening diameter
\tilde{D}	Crack driving state function
E_{ac}	Activation energy for hydration
E_c	Elastic modulus
E_∞	Elastic modulus at fully hydrated state
f_c	Compressive strength
f_t	Tensile strength
f_∞	Compressive strength at fully hydrated state
\hat{f}_d	Diffusion
$\hat{g}(d)$	Degredation function
G_c	Critical energy release rate
h	Moisture
$\hat{\mathcal{H}}_d$	Crack driving force
\mathbf{I}	Linear momentum
l	Length scale
\mathcal{L}	Crack phase field localization zone
n	Gradation index
$P(d)$	Cumulative percentage passing
\hat{q}_d	Resistance to the crack phase field evolution
R	Universal constant for ideal gases
R_{agg}	Area ratio of coarse aggregates

T	Temperature
T_{max}	Maximum temperature
T_{min}	Minimum temperature
T_{ref}	Reference temperature
\mathbf{u}	Displacement field
u_i	Longitudinal direction
v_i	Transverse direction
w/c	Water-cement ratio
X_0	X value of a random location of an aggregate
X_{max}	Maximum x value of the cross section
X_{min}	Minimum x value of the cross section
Y_0	Y value of a random location of an aggregate
Y_{max}	Maximum y value of the cross section
Y_{min}	Minimum y value of the cross section
α	Phase angle
$\beta(h)$	Function related with moisture effects on the hydration
β	Ratio of maximum principal stress to the instantaneous tensile strength
γ_l	Crack surface density function
$\boldsymbol{\varepsilon}$	Strain tensor
$\boldsymbol{\varepsilon}^{sh}$	Shrinkage strain tensor
η	Material parameter related with hydration
η_i	Uniformly distributed random number between 0 and 1
η_x	Model parameter related with aging
θ_i	Polar angles
Θ_i	Subtended angles
κ	Ratio of the prescribed elongation ratio to the original elongation ratio
$\hat{\lambda}(\chi)$	Lamé constant
$\hat{\mu}(\chi)$	Shear modulus

ν	Poisson's ratio
ξ	Degree of hydration
σ	Stress tensor
χ	Aging degree
ψ	Energy storage function
ψ_c	Energy storage function threshold

CHAPTER 1

INTRODUCTION

Concrete is a construction material that is broadly used in structures such as residential buildings, dams, pavements, and power plants. Therefore, the comprehension of its behavior is vital. The behavior of mature concrete is significantly affected by its early-age history. Young concrete goes through hardening and gains its strength and rigidity through the hydration of cement. While the hydration process takes place under various conditions, the shrinkage of concrete occurs. Subsequently, the shrinkage may lead to micro-cracks, and during the lifetime of concrete, micro-cracks may build up to macro-cracks so that failure may occur. Therefore, this work is concerned with the computational modeling of hardening concrete at mesoscale where the effects of aggregate geometry, aggregate roundness, grading, and the amount of shrinkage on the evolution of the residual stresses are investigated. Furthermore, in the subsequent strength prediction through the phase-field fracture analyses on the various hardened mesostructures, the ultimate influence of the investigated factors on the tensile strength of concrete is investigated.

1.1 Hydration of Concrete

Concrete is a widely preferred material in construction. Its popularity is due to its ability to achieve required high-strength values. The strength and rigidity of concrete are characterized by hydrated cement, aggregates, and the interfacial transition zone (ITZ) between aggregate and cement paste. Concrete gains its strength and rigidity throughout its lifetime, but the early ages are more crucial regarding the contribution of its strength gain. The mechanism of strength gain of young concrete is called hard-

ening. Hardening is caused by a set of exothermic chemical processes that is named hydration. During hydration, cement reacts with water to form the compounds that are referred to as hydrates. Unhydrated cement is reached by the water that diffuses through the layers of hydrates. Therefore, the moisture distribution within the material plays a crucial role in the hydration process. The moisture content decreases by drying of concrete and also by the water consumption through hydration, the so-called self-desiccation.

The initiation of hydration occurs quickly as soon as the water contacts with cement. As the hydration begins, a great amount of heat is liberated, and until the hydration process is finished, heat liberation continues. However, the process does not attain 100% level of completion, so the strength and rigidity gain still continues in the mature concrete. The release of heat causes a temperature difference between both hydrates and aggregate and hydrates and unhydrated cement. The mismatch between the temperatures provokes the initiation of micro-cracks.

Cement is composed of five main minerals. These are aluminates: tricalcium aluminate (C_3A) and tetracalcium aluminoferrite (C_4AF); silicates: tricalcium silicate (C_3S), dicalcium silicate (C_2S), and calcium sulfate ($C\bar{S}$), which is also known as gypsum. The primary compounds of hydration is calcium silicates that constitutes about 75% of cement.

During the initial stage of hydration of cement, water comes into contact with cement particles that causes rapid dissolution of C_3A and $C\bar{S}$ (gypsum). Within about 15 minutes, these materials produce solid compounds that results in significant heat generation that increases rapidly. During this period, a reaction between fast-dissolving gypsum, dissolved C_3A , and water produces a substance that coats the cement grains. This hydration product, known as a gel-like ettringite ($C-A-\bar{S}-H$), is solid but lacks a specific composition or crystalline form. It slows down the aluminate reactions, thereby reducing the amount of heat generated by the end of the mixing stage [5].

Within 1–3 hours after the mixing stage, the second stage of cement hydration occurs. During this stage, the gel-like substance known as $C-A-\bar{S}-H$ controls the aluminate reactions, resulting in a deceleration of heat generation. As the cement continues to dissolve, the water becomes saturated with dissolved calcium and hydroxyl (OH) ions, but the dissolution of silicates happens at a slower rate. By the end of the second stage, the water becomes fully saturated with calcium ions, and the hardening process

begins [5].

The third stage begins once the concrete starts to set. In this stage heat of hydration rate increases. C_3S governs this stage and calcium silicate hydrate and calcium hydroxide form as the results of reaction of silicates and water. C-S-H, which is the desired hydration product due to its contribution of strength and rigidity gain of concrete, is resulted in both from the reactions of C_3S and C_2S with water.

In the fourth stage of the cement hydration process, the reactions between water and undissolved cement particles persist, while the reaction rate of C_3S decreases. This leads to an increase in heat generation rate, followed by a gradual slowdown. After the temperature reaches its peak, $C\bar{S}$ reacts continuously with aluminates. The remaining aluminates react with ettringite to form monosulfate, which has no significant impact on the properties of the resulting concrete [5].

In the fifth stage of hydration, the rate of strength and rigidity gain in concrete slows down, approaching a steady state, marking the hardened state of the material. The remaining C_3S will continue to react with water, forming C-S-H. Both C_3S and C_2S react with water, with C_3S reacting primarily before C_2S becomes notable [5].

Many experimental and computational studies have been conducted on the hydration of concrete. A thermo-chemo-mechanical coupling model is studied by Ulm and Coussy [27] with the identification of thermodynamic force and maturity, which are called the chemical affinity and the degree of hydration, respectively, as the internal variables. The missing effects of the evolution of stress and temperature are included in the work of Cervera et al. [5] with the consideration of hydration kinetics. They introduced an internal variable named the degree of aging that the mechanical properties of concrete are evolved by.

Gawin, Pesavento, and Schrefler [6, 7] introduced an early-age model that considers solidification and they extended it to a hygro-thermo-chemo-mechanical model. Di Luzio and Cusatis [8, 9] included moisture transportation and heat transfer with a calibrated and validated hygro-thermo-chemical model.

Apart from the computational studies that model hydration kinetics, some studies experimentally measure the degree of hydration. Bouasker et al. [10] measured the degree of hydration of cement paste with thermogravimetric analysis, which is a method that determines the degree of hydration by measuring the amount of product that is burned [11], and the degree of hydration of mortar by loss on ignition, which is a

method that is based on the weight loss of the unhydrated cement [11]. Zhang et al. [11] determined the degree of hydration through thermogravimetric analysis and they also relate the degree of hydration with the percolation threshold, i.e. setting point, with ultrasonic velocity measurements.

1.2 Shrinkage of Concrete

Shrinkage is a volumetric deformation that takes place over time. It can be classified into different types, such as drying shrinkage, plastic shrinkage, autogenous shrinkage, and chemical shrinkage. Drying shrinkage is the evaporation of excess water from the surface after the concrete has hardened. Plastic shrinkage is associated with the loss of water from the surface due to poor curing at early ages. Autogenous and chemical shrinkage are related to water consumption through the hydration process, and self-desiccation.

There is a lack of agreement on the applied terminology about chemical and autogenous shrinkage. Jensen and Hansen [12] described autogenous shrinkage as the internal volume reduction due to hydration reactions and chemical shrinkage as the bulk deformation of a close, isothermal system that is not subjected to external forces. Shrinkage of concrete leads to cracking when it is subjected to restraints such as differential shrinkage or aggregate. Differential shrinkage may occur due to the fact that the liberated heat by the hydration may be differential in the concrete. Aggregates have a restraining effect on shrinkage and that will eventually lead to microcracks [13].

Experimental studies have been widely conducted on drying shrinkage [14–16], plastic shrinkage [17–19] of cement and mortar. Considering the point of view of our work, it is more relevant to take into consideration of studies regarding chemical and autogenous shrinkage and their direct relation to the degree of hydration. Bouasker et al. [10], which is also mentioned in Section 1.1, measured volumetric chemical shrinkage while relating it to the measured degree of hydration. Also, Zhang et al. [11] assess the chemical shrinkage while relating it to the degree of hydration of oil-well cement under different temperatures and have similar findings to the work of Bouasker et al. [10]. Fu et al. [20] suggested an equation regarding autogenous

shrinkage and creep according to the findings of the conducted tests. Bentz et al. [2] conducted experiments for comparing the early-age strength of mortars with 0.35 water-cement ratio prepared with cement having different fineness values and the autogenous shrinkage is measured between 100–300 microstrains, Figure 1.2. Findings of Bentz et al. [1] are also similar to that of Bentz et al. [2], who conducted experiments to examine the effect of shrinkage reducing admixtures and they measured autogenous shrinkage of mortar having 0.35 water-cement ratio between 100 – 300 microstrains, Figure 1.1. Autogenous shrinkage measurements of Loukili et al. [3] for mortar having water-cement ratio of 0.35 is also presented at Figure 1.3. Although the measurement values are not relatively close enough, the findings of Lu et al. [4], Figure 1.4, show that having different proportions of sand in mortar specimens results in such values.

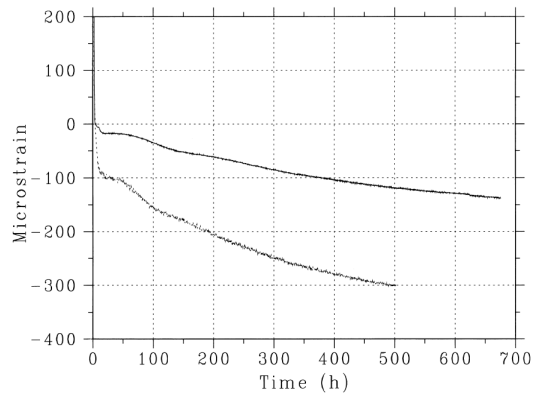


Figure 1.1: Autogenous shrinkage findings of Bentz et al. [1] with and without Shrinkage Reducing Admixture

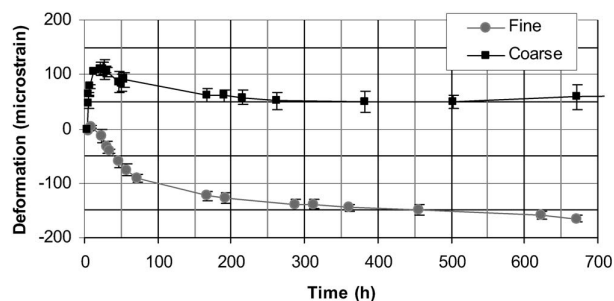


Figure 1.2: Autogenous shrinkage findings of Bentz et al. [2] with fine and coarse aggregates

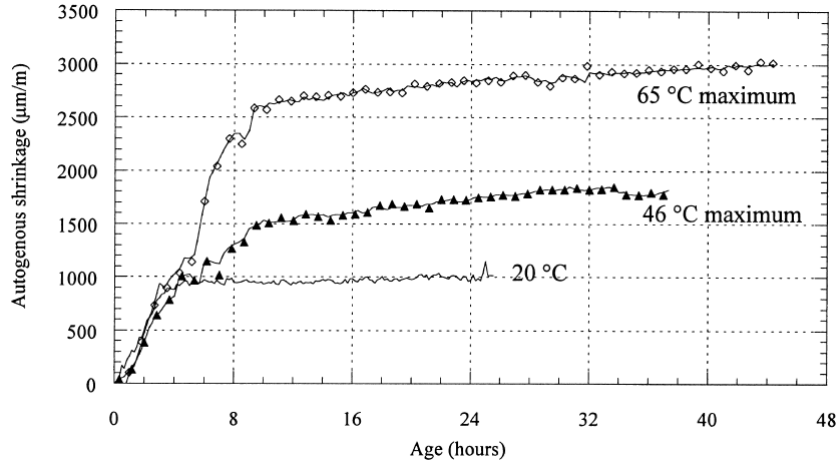


Figure 1.3: Autogenous shrinkage findings of Loukili et al. [3]

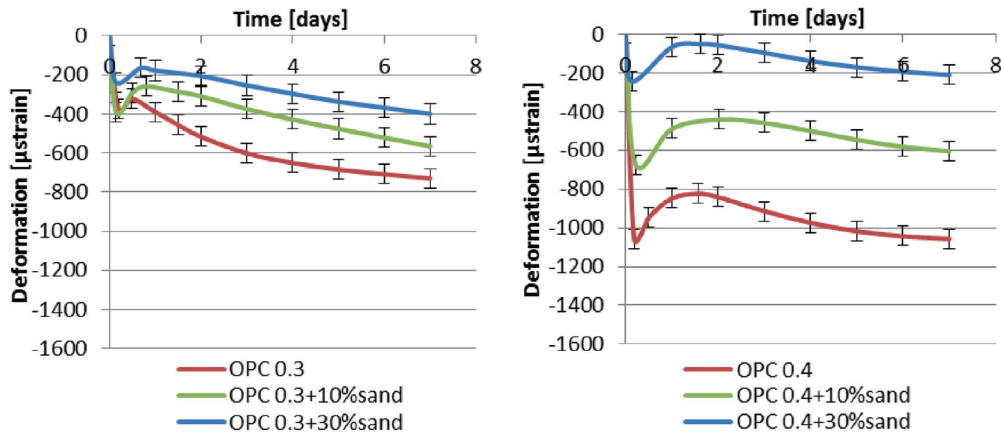


Figure 1.4: Autogenous shrinkage findings of Lu et al. [4] for w/c ratio of 0.3 and 0.4 for different percentage of sand

1.3 Meso-Structure and Concrete

Concrete is a composite material that consists of Portland cement, sand, coarse aggregates, and water. The heterogeneity of concrete could differ according to the scale that the material is examined. Although concrete is treated as a homogenous material at macroscale, it is scrutinized as a heterogeneous material composed of Portland cement, sand, coarse aggregates, and water at microscale. At mesoscale, concrete is studied as a heterogeneous material that includes mortar with sand dissolved in it,

coarse aggregate, and the interfacial transition zone between coarse aggregates and mortar. The multi-phase structure of concrete that is represented by meso-scale modeling helps us understand the non-linear behavior of concrete. The different mechanical properties of each of these phases provide a better examination of the relationship between phases and their contribution to the overall concrete behavior.

The assessment of modeling concrete at different scales could be addressed to the level of detail and the computational cost. Microscale modeling enables to understand the behavior of concrete regarding the fundamental mechanism of individual particles and the relations between them. The approach causes modeling at the microscale to be computationally costly due to its detailed inspection. On the other hand, modeling at mesoscale simulates the general behavior of the material, and it is more efficient computationally since it inspects in less detail than microscale modeling.

The generation of a meso-structure could either be done by computationally constructing an existing structure or by generating a random meso-structure (RMS). X-ray computed tomography or CT-scanning specimens [21] is a way of constructing an existing structure. It has the advantage of modeling the structure realistically. The numerical result of an analysis of the structure may be more accurate as it eliminates any oversight that could be made by imitating a real structure. A meso-structure could lack representing a realistic structure if the model is simplified extensively. However, an accurate representation of a meso-structure provides a way to control how different variables, such as aggregate shape, position, and segregation, affect the development of residual stresses while concrete is going through hardening and shrinkage.

The method of Take-and-Place [22] is a technique for generating a RMS or, in this case, the random aggregate structure where the geometry, size, and distribution of aggregates closely mimic the real concrete statistically. The method generates randomly shaped and randomly placed aggregates with respect to a grading curve in a section. The generation of a RMS gives the ability to control various parameters and facilitates seeing how the analysis results are affected by a specific parameter change.

Modeling concrete at mesoscale is widely used in the literature primarily the investigation of aggregate shape, size, and distribution [23–25]. The damage and failure of concrete are studied with the introduction of a damage parameter [26–30] at mesoscale. Also, the propagation and initiation of crack is modeled using phase-field [31–33].

Over the past few years, there has been a growing interest in studying the development of residual stresses considering different phenomena of early-age concrete and the impact of residual stresses on the long-term performance of hardened concrete. Corrado and Molinari [34] investigated the propagation of cracks under the influence of residual stresses that are developed under drying shrinkage of mortar. They represented the cracks by dynamically inserting cohesive zone elements during the simulation. Xu et al. [35] studied the development of self-restrained thermal stresses that are due to the heat released from the hydration reaction of hardening concrete considering elastic strain, creep strain, thermal strain, and autogenous strain. They conducted analyses in 3-D with spherical aggregate particles. Nguyen et al. [36] examined the early-age cracking of hardening concrete with a phase-field model considering thermal expansion strain, autogenous shrinkage strain mesoscale, transient thermal creep strain, and basic creep strain. Li et al. [37] examined the early-age hydration considering heat transfer, humidity transport, and chemical reactions. They investigated the effects of relative humidity, area ratio and shape of the aggregates on the development of principal stresses. They also validated their model with the experiments they conducted for concrete model with and without the presence of expansion agent, mortar model without any agent. Taibi et al. [38] investigated the hardening process of mass concrete, taking into account the effects of autogenous and thermal strains using damage plasticity model in 2-D. Their study also examined how a pipe cooling system impacts the behavior of concrete at mesoscale and the effect of early-age hydration on the mechanical behavior of hardened concrete using simplified morphology of circular aggregates. Qiu et al. [39] enhance the model Xu et al. [35] used by considering the complex morphology of actual aggregates. They investigated the effects of aggregate morphology and orientation on stress concentrations by relating it with the thermal effects of hardening concrete. Qiu et al. [40] examined the effects of residual stresses, which are obtained by using their previously mentioned work [39], on the mechanical response of hardened concrete with a elasto-viscoplastic damage model. They used diffuse meshing technology to represent ITZ.

1.4 Scope and Aim of the Thesis

This study aims to model the hardening phenomenon in concrete considering hydration and shrinkage of mortar at mesoscale. The effect of the produced stresses, which are referred as the residual stresses, due to hardening of concrete is investigated under different mechanical loadings and crack formation is examined using the phase-field fracture model and cohesive zone elements. Although the residual stresses may seem insignificant, they characterize the overall performance of concrete.

A model is developed to consider the hydration effects by relating it to the mechanical parameters of the material. It is crucial to take into account the shrinkage effects while associating it with the hydration process since, during the early hydration, material may be significantly affected by shrinkage strain. To make use of the developed models, a tool for the generation of random meso-structures is implemented. The tool is used to assess the impact of different factors of aggregate on the development of principal stresses and their ratio to the tensile strength of mortar. These factors are the roundness, shape, area ratio, grading, and segregation of aggregate.

ITZ, located between the aggregate and mortar, is included in this work using cohesive zone elements. With the cohesive zone elements and the phase-field fracture model the crack formation is observed in the presence and absence of residual stresses. Although there are comprehensive works, which are mentioned in Section 1.3, regarding the hydration and hardening of concrete; this work is one of the pioneers that examines the mesostructure of concrete under initial residual stresses, due to hydration of mortar, using cohesive zone elements and the phase-field fracture model to observe crack formation and propagation.

1.5 Outline of the Thesis

The rest of the thesis is organized as follows. In Chapter 2, the construction of the randomly shaped aggregates, the taking process, and the placing process are discussed. In Chapter 3 the governing balance equations, the associated boundary conditions, and the constitutive equations along with the hydration and aging mechanism are described. In Chapter 4 the representative numerical examples are presented along with

the results and discussions based on the computationally obtained results. In Chapter 5 concluding remarks are given.

CHAPTER 2

GENERATION OF RANDOM MESO-STRUCTURES

Random meso-structures (RMS) are generated to realistically represent multi-phase composite structures. The Take-and-Place Method, which is the implemented method for this work according to the study of Wang et al. [22], is one of the widely used methods to generate RMS in a statistical manner. The generated structure should resemble a homogenous material on the macroscale where the randomness of geometric arrangements should be met. To be able to fulfill these needs the Take-and-Place method, which is based on the Monte-Carlo sampling technique, is used. By taking samples from a source and placing them in a section, by avoiding overlapping, randomness is applied.

2.1 Generation of Polygonal Aggregate Particles

Fine and coarse aggregates are the two types of aggregates that concrete sections consist of. Generally, aggregates smaller than 4.75 mm are assumed to be fine and the bigger ones are considered to be coarse aggregates. In a meso-scale analysis, fine aggregates are taken into account as a part of the matrix. In this work, a prescribed shape of a coarse aggregate is generated.

Polygons are constructed using polar coordinates. A polygon's vertices, a total of n , are represented by polar radius, r , and polar angles, θ . It has been stated from visual interrogations that aggregates generally have between 4 and 10 vertices. But having vertices between 4 and 10 results in relatively sharp corners and constructing a shape of an aggregate beyond these limits also results in sharp corners. Therefore, first, a random number between 4 and 10 is generated to be assigned to the number

of vertices of an aggregate. Then, after constructing the shape of the aggregate, the cubic spline is fitted to smooth out the sharp corners.

While constructing the shape of an aggregate, subtended angles, defined as $\Theta_i := \theta_{i+1} - \theta_i$, are used. To obtain a polygonal shape, the mean value of the subtended angles should be $2\pi/n$. The subtended angles, presented in Figure 2.1 could be obtained as formulated in (2.1) where δ represents the variation, which is always less than 1, from the mean and η_i represents a uniformly distributed random number between 0 and 1.

$$\Theta_i = \frac{2\pi}{n} + (2\eta_i - 1)\delta\frac{2\pi}{n} \quad (2.1)$$

Since the sum of the angles should be exactly 2π a correction should be made as

$$\bar{\Theta}_j = \Theta_i \frac{2\pi}{\sum_{j=1}^n \Theta_j}, \quad (2.2)$$

and the polar angles, also presented in Figure 2.1, could then be obtained as

$$\theta_i = \sum_{j=1}^{i-1} \bar{\Theta}_j. \quad (2.3)$$

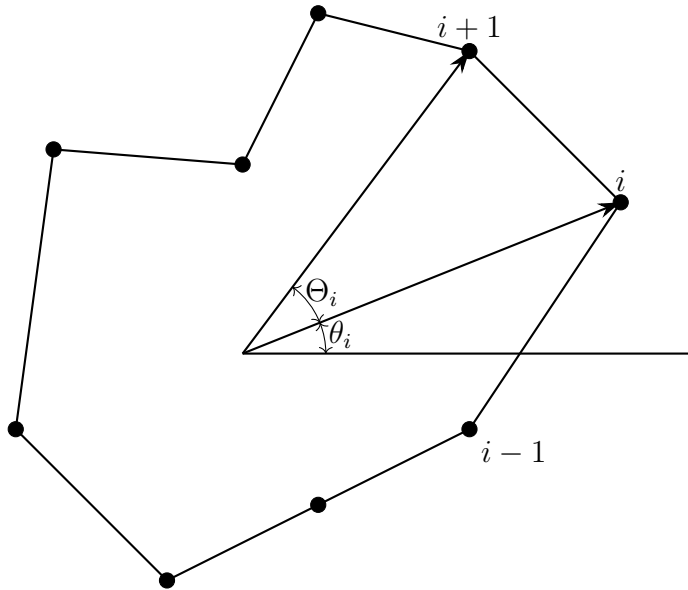


Figure 2.1: An aggregate with its polar coordinates and angles

The generation of a prescribed shape could be achieved after an adjustment of vertices as the generated shape could have a different elongation ratio than the prescribed one.

The width and the length of the aggregate are described as follows: the width is the width of the rectangle that has minimum width among every rectangle that is obtained by the rotation of the aggregate. The length is the length of the same rectangle. To generate such a rectangle; first, all the vertices that violate the convexity of the polygon are eliminated. After the elimination, a rectangle is constructed by taking a side of the rectangle as an edge of the polygon and the rectangle should be just big enough to contain all the vertices of the polygon. This process is repeated for every edge of the convex polygon. Last, after constructing every rectangle for each edge, the one having the minimum width is selected and its width and length are assigned to the aggregate. By obtaining these values, the elongation ratio could finally be calculated. Then, the shape is adjusted to the prescribed value and the original elongation ratio to become the same by stretching or compressing the polygon. The adjustment,

$$\bar{u}_i = \kappa u_i, \quad (2.4)$$

is made by multiplying the longitudinal direction of the Cartesian coordinates, u_i , with a ratio, κ , defined as the ratio of the prescribed elongation ratio to the original elongation ratio. The adjustment is not applied in transverse direction it is only been applied in longitudinal direction,

$$\bar{v}_i = v_i. \quad (2.5)$$

2.1.1 Grading of Aggregate

Aggregate size distribution, i.e. grading, is generally taken as the cumulative percentage of aggregates that passes through a series of sieve sizes. The Fuller curve [41], one of the grading curves that have optimum density, is used in this work and it could be calculated as

$$P(d) = 100 \left(\frac{d}{d_{max}} \right)^n, \quad (2.6)$$

where $P(d)$ represents the cumulative percentage passing, d is the related opening diameter, d_{max} is the maximum opening diameter, n is the gradation index. Total area, $A_{agg}[d_s, d_{s+1}]$, between two opening sizes, $[d_s, d_{s+1}]$ could be obtained as

$$A_{agg}[d_s, d_{s+1}] = \frac{P(d_{s+1}) - P(d_s)}{P(d_{max}) - P(d_{min})} R_{agg} A_{con}, \quad (2.7)$$

where R_{agg} is the area ratio of coarse aggregates and A_{con} is the area of the cross section.

2.2 Take-and-Place Method

The Take-and-Place method is used for simulating a real specimen in a statistical manner. It has the ability to represent the model as homogenous on a macroscale while constructing a mesoscopic heterogeneous structure. It includes two processes that happen concurrently for every particle. The first one, the take-process, includes "taking" a particle from a source whose total area is calculated according to the grading curve and shaping the particle. The latter, the place-process, is related to "placing" of the particle in the section so that it will not intersect or overlap with already placed particles.

2.2.1 Take-Process

Take-process is initiated from the segment that has the biggest size and continues with the smaller ones. The process could be explained with the following steps:

1. Calculate the total area of particles that could be generated according to the related grading segment.
2. Generate the shape of the particle using the necessary random numbers
3. Execute the Place-Process
4. Repeat the previous two steps until the area of the next aggregate that could be generated with the minimum size obtained from the related segment is bigger than the total area calculated in Step 1.
5. Move to the next grading segment and return to Step 1 until all segments are covered.

2.2.2 Place-Process

While executing the placing process, first, a random location, Point 0, within the cross-section is obtained using,

$$X_0 = X_{min} + \eta_1 (X_{max} - X_{min}) \quad (2.8)$$

$$Y_0 = Y_{min} + \eta_2 (Y_{max} - Y_{min}), \quad (2.9)$$

where X_0 and Y_0 are the coordinates of the Point 0; X_{max} , Y_{max} , X_{min} , Y_{min} are the maximum and minimum X , Y values of the cross section where aggregates are placed; η_1 and η_2 values are two uniformly distributed random values between 0 and 1 and independent from each other.

Then; the phase angle α , which is the angle defines the orientation of particle, is calculated as

$$\alpha = \eta \cdot 2\pi, \quad (2.10)$$

where η is a uniformly distributed random number between 0 and 1.

Table 2.1: Steps of Take-Process and Place-Process

Take-Process	Place-Process
<p>T1. Calculate the total area of particles that could be generated according to the related grading segment.</p> <p>T2. Generate the shape of the particle using the necessary random numbers.</p> <p>T3. Execute the Place-Process</p> <p>T4. Repeat the previous two steps until the area of the next aggregate that could be generated with the minimum size obtained from the related segment is bigger than the total area calculated in T1.</p> <p>T5. Move to the next grading segment and return to T1 until all segments are covered.</p>	<p>P1. Generate the shape of the aggregate</p> <p>P2. Generate the location of the aggregate.</p> <p>P3. Generate the phase angle of the aggregate</p> <p>P4. Check whether the aggregate can be placed to the generated location if it can return to T4 if it cannot continue to P5.</p> <p>P5. If the total trial amount is a integer multiple of 100 return to P2, if the total trial amount is above 1000 return P1 and reset the trial amount to 0, if the previous two conditions are false return to P3.</p>

After the determination of the location and the angle of the particle, it is checked if the aggregate could be placed in that spot. This operation includes two checks. The first one is checking if the particle is within the boundary of the cross-section. The second one is checking if the particle intersects or overlaps any other particle already placed. Whole process of Take-and-Place Method is given in Table 2.1 The aggregate placement of each segment of the grading curve is shown in Figure 2.3 with color coding that is compatible with Figure 2.2. Since aggregate smaller than 5 mm is considered fine aggregate the grading curve is presented for aggregate bigger than 5 mm.

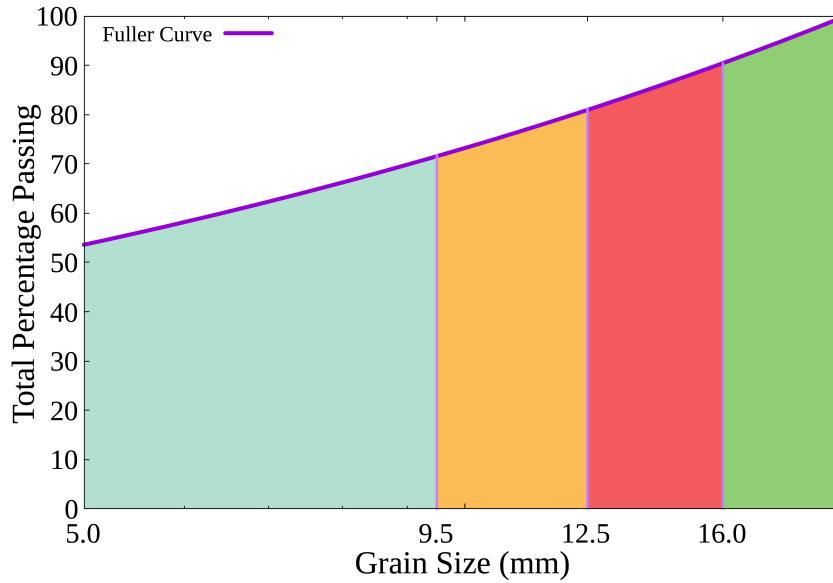


Figure 2.2: The grading curve

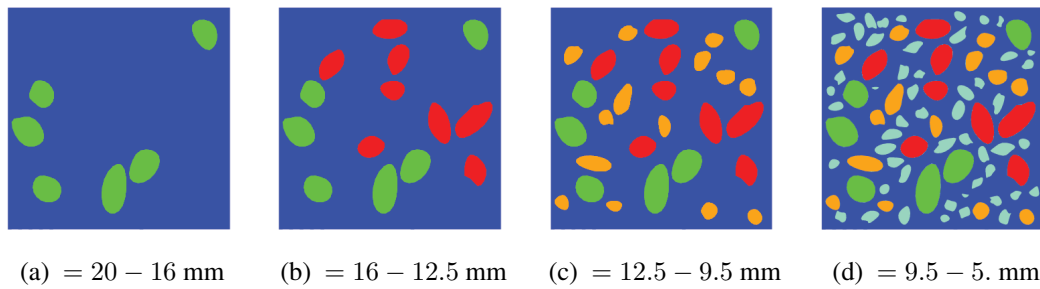
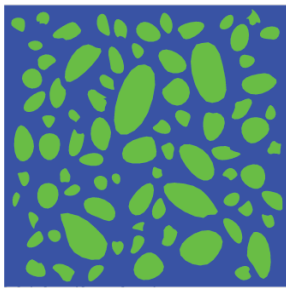


Figure 2.3: Stages of aggregate placement. The colors of aggregates indicate the corresponding grading interval in Figure 2.2

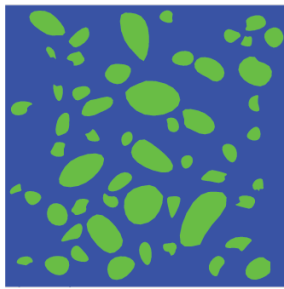
2.3 Generated Structures

Some examples of the generated structures that are also used in numerical examples in Section 4 are presented in Figure 2.4. The dimensions of all the generated sections are 150 mm \times 150 mm. Related parameter information is also presented in Table 4.4. Case I in Figure 2.4 represents a control case, in Case II and III the area ratio of aggregates is investigated, Case IV is related with the segregation, in Case V the elongation ratio of aggregate is examined, and in Case VI, a control case, and Case

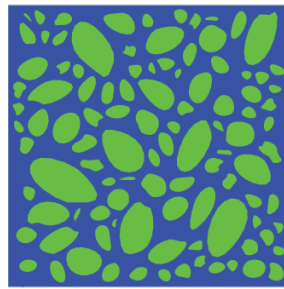
VII the roundness of aggregate is discussed.



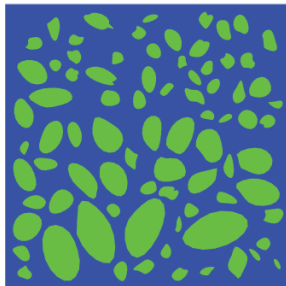
a) Case I



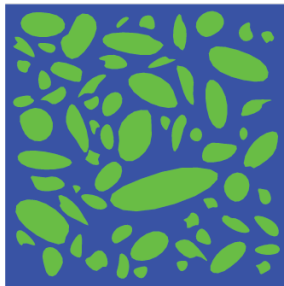
b) Case II



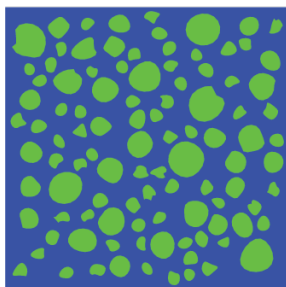
c) Case III



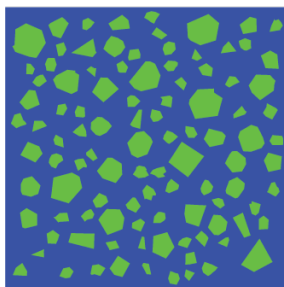
d) Case IV



e) Case V



f) Case VI



g) Case VII

Figure 2.4: Random meso-structures generated

CHAPTER 3

GOVERNING AND CONSTITUTIVE EQUATIONS

The exothermic nature of hydration results in a significant temperature rise in the concrete body. The surface of mass structures cools at a faster rate, leading to a nonuniform distribution of temperature that leads to thermally induced volumetric deformations. Although thermally induced volumetric deformations are not so relevant in comparatively small structures, autogenous volumetric deformation can be critical in both massive and comparatively small structures. Autogenous shrinkage is related with the so called self-desiccation that is the internal water consumption during hydration that leads to volumetric deformation. Thus, the modeling of the hardening process is significant due to the volumetric deformation of the concrete may results in cracking. Although the deformations that occur during the hardening process of concrete are small in comparison to the life-time deformations that it undergoes, it is during this time that concrete is gaining rigidity and strength and is therefore particularly vulnerable to deformations. The vulnerability of concrete during the hardening process comes from both its lack of fully strength and its rapidly changing material properties. Therefore, it is crucial to properly model this sensitive process. In this work only autogenous deformations are taken into account since the examination of comparatively small structures has been conducted.

Hydration of concrete throughout the hardening process is a primary cause of the mentioned volume changes. Due to the heterogeneity of the structure of concrete at mesoscale and the constraints on it, the change in volume may cause the evolution of residual stresses and the formation of micro-cracks in the specimen during hardening. Although the micro-cracks seem small at first, throughout the life time of concrete, these micro-cracks may lead up to macro-cracks under different loading conditions. The phase-field method, a variational numerical method, has been introduced and

been widely adopted. It allows for the development of models at different scales and also enables the representation of complex crack topologies, whose thickness can be controlled with a length scale parameter, by introducing an additional phase-field variable. The additional variable eliminates the remeshing problem for the simulation of crack growth.

In this chapter the key equations are presented regarding the mechanical behavior of hardening concrete. In Section 3.1 kinematics and state variables; the strain tensor, the crack phase field for brittle fracture, and the degree of hydration are introduced. In Section 3.2 governing balance equations are described. The stress response is introduced using the degradation function in Section 3.3. The crack driving force and its incremental update scheme are presented in Section 3.4. Last, the hydration of cement and its aging mechanism are discussed paying regards to work of Di Luzio and Cusatis [42] in Sections 3.5 and 3.6.

3.1 Kinematics and State Variables

Assume a configuration of a material body in the Euclidian space, $\mathcal{B} \subset \mathbb{R}^3$, at time $t \in \mathcal{T}$. The displacement field \mathbf{u} of a material point positioned at $\mathbf{x} \in B$, and time $t \in \mathcal{T}$ is described by

$$\mathbf{u} := \begin{cases} \mathcal{B} \times \mathcal{T} \rightarrow \mathbb{R}^\delta \\ (\mathbf{x}, t) \mapsto \mathbf{u}(\mathbf{x}, t), \end{cases} \quad (3.1)$$

in the geometrically linear setting. Then, the strain tensor can be expressed as the symmetric displacement gradient,

$$\boldsymbol{\varepsilon}(\mathbf{u}) = \nabla \mathbf{u} := \frac{1}{2}[\nabla \mathbf{u} + \nabla^T \mathbf{u}]. \quad (3.2)$$

To consider stress degradation only in tension, the strain tensor is decomposed into its positive and negative parts

$$\boldsymbol{\varepsilon} = \boldsymbol{\varepsilon}_+ + \boldsymbol{\varepsilon}_- \quad (3.3)$$

where $\boldsymbol{\varepsilon}_+$ and $\boldsymbol{\varepsilon}_-$ are defined using the spectral decomposition of the strain tensor, $\boldsymbol{\varepsilon} = \sum_{i=1}^3 \epsilon_i \mathbf{n}_i \otimes \mathbf{n}_i$ where $\epsilon_{1,2,3}$ denote the principal strains and $\mathbf{n}_{1,2,3}$ are the principal

directions. The positive and the negative parts of the strain tensor are then given by

$$\boldsymbol{\varepsilon}_+ := \sum_{i=1}^3 \langle \varepsilon_i \rangle_+ \mathbf{n}_i \otimes \mathbf{n}_i \quad \text{and} \quad \boldsymbol{\varepsilon}_- := \sum_{i=1}^{\delta} \langle \varepsilon_i \rangle_- \mathbf{n}_i \otimes \mathbf{n}_i \quad (3.4)$$

where the Macaulay bracket operators are defined as

$$\langle x \rangle_+ := (x + |x|)/2 \quad \text{and} \quad \langle x \rangle_- := (x - |x|)/2. \quad (3.5)$$

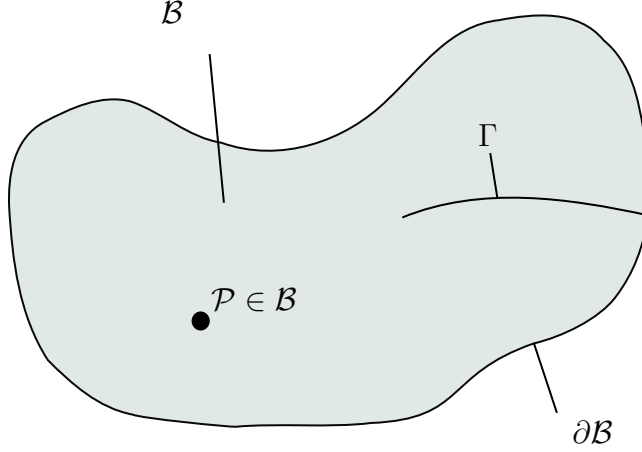


Figure 3.1: Sharp crack embedded in a solid body

Approximation of the total surface area of a sharp crack Γ in the body \mathcal{B} , as demonstrated in the Figure 3.1,

$$\mathcal{S} := \int_{\Gamma} dA \approx \int_{\mathcal{B}} \gamma_l(d, \nabla d) dV \quad (3.6)$$

depends on the crack phase field d and its gradient ∇d . The phase-field values vary within the interval $d \in [0, 1]$ where the lower bound represents intact state and the upper bound represents the fully broken state.

The crack surface density function can be defined as

$$\gamma_l(d, \nabla d) := \frac{1}{2l} d^2 + \frac{l}{2} |\nabla d|^2 \quad (3.7)$$

where the length scale parameter, l , controls the width of the crack. Sharp crack topologies could be obtained by choosing a small length scale parameter as shown in Figure 3.2. Thus, the length scale, l , has a significant effect on the behavior of material response.

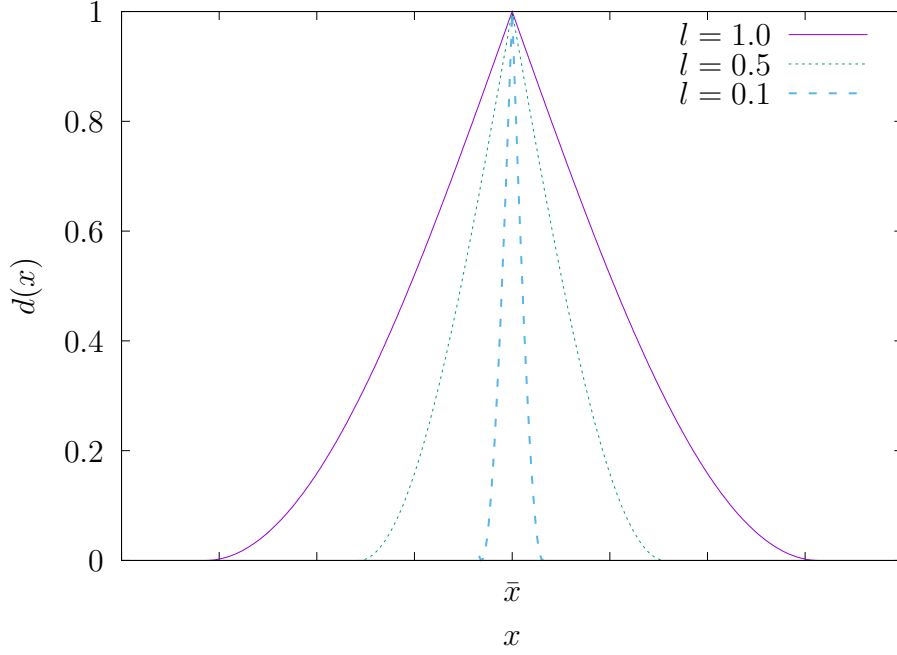


Figure 3.2: Phase-field approximations with different length scale values

The state of the material,

$$\text{State}(\mathbf{x}, t) = \{\mathbf{u}(\mathbf{x}, t), d(\mathbf{x}, t), \xi(\mathbf{x}, t)\}, \quad (3.8)$$

is constituted by the displacement field, $\mathbf{u}(\mathbf{x}, t)$, the crack phase field, $d(\mathbf{x}, t)$, and the degree of hydration, $\xi(\mathbf{x}, t)$, which indicates the extend of hydration of the material.

3.2 Governing Equations

Newton's second law of motion, the conservation of linear momentum principle,

$$\frac{d\mathbf{I}}{dt} = \mathbf{F}, \quad (3.9)$$

states that the rate of change of linear momentum of a body part \mathcal{P} over time is equal to the net force acting on it. The linear momentum is defined as

$$\mathbf{I} = \int_{\mathcal{P}} \rho \mathbf{v} dV \quad (3.10)$$

and the mechanical force \mathbf{F} mentioned in (3.9) is given as

$$\mathbf{F} = \int_{\mathcal{P}} \rho \mathbf{b} dV + \int_{\partial\mathcal{P}} \mathbf{t} dA. \quad (3.11)$$

Using (3.10) and (3.11) the conservation of linear momentum, (3.9), can be expressed as

$$\frac{d}{dt} \int_{\mathcal{P}} \rho \mathbf{v} dV = \int_{\mathcal{P}} (\dot{\rho} \mathbf{v} + \rho \dot{\mathbf{v}}) dV = \int_{\mathcal{P}} \rho \mathbf{b} dV + \int_{\partial \mathcal{P}} \mathbf{t} dA. \quad (3.12)$$

With the utilization of the Cauchy's theorem and the Gauss integral theorem, the surface integral in (3.12) becomes

$$\int_{\partial \mathcal{P}} \mathbf{t} dA = \int_{\partial \mathcal{P}} \boldsymbol{\sigma} \mathbf{n} dA = \int_{\mathcal{P}} \operatorname{div}(\boldsymbol{\sigma}) dV. \quad (3.13)$$

Substituting (3.13) into (3.12) along with the conservation of mass, we arrive at

$$\int_{\mathcal{P}} (\rho \mathbf{a} - \operatorname{div}(\boldsymbol{\sigma}) - \rho \mathbf{b}) dV = 0. \quad (3.14)$$

The localization of (3.14),

$$\lim_{\mathcal{P} \rightarrow dV} \int_{\mathcal{P}} (\rho \mathbf{a} - \operatorname{div}(\boldsymbol{\sigma}) - \rho \mathbf{b}) dV = \mathbf{0}, \quad (3.15)$$

results in the local form of the conservation of linear momentum,

$$\rho \mathbf{a} = \operatorname{div}(\boldsymbol{\sigma}) + \rho \mathbf{b}. \quad (3.16)$$

The rate of the crack surface density, which is introduced in (3.7) can be described as

$$\dot{\gamma}_l(d, \nabla d) = \delta_d \gamma_l \dot{d} \quad \text{with} \quad \delta_d \gamma_l := \partial_d \gamma_l - \operatorname{div}(\partial_{\nabla d} \gamma_l) \quad (3.17)$$

holding for homogeneous Neumann boundary conditions, $\partial_{\nabla d} \gamma_l \cdot \mathbf{n}_{\mathcal{L}} = 0$, on $\partial \mathcal{L}$ where $\mathbf{n}_{\mathcal{L}}$ is the outward unit normal function and \mathcal{L} is the crack phase field localization zone. The variational derivative of (3.7) can then be obtained as

$$\delta_d \gamma(d) := \partial_d \gamma - \operatorname{div}[\partial_{\nabla d} \gamma] = \frac{1}{l} [d - l^2 \Delta d]. \quad (3.18)$$

Making use of the local dissipation, (3.18), and the irreversibility condition, $\dot{d} > 0$, the following nonlocal damage evolution expression can be obtained,

$$\operatorname{div}(\hat{\mathbf{q}}_d) - \hat{\mathcal{H}}_d + \hat{f}_d = 0 \quad (3.19)$$

where $\hat{\mathcal{H}}_d$ is the crack driving force, $\hat{\mathbf{q}}_d$ and \hat{f}_d define the resistance to the crack phase field evolution and diffusion. The latter are defined as

$$\hat{\mathbf{q}}_d = -l G_c \nabla d, \quad \hat{f}_d = \frac{G_c}{l} d, \quad (3.20)$$

where G_c is the critical energy release rate. Thus, the balance equations (3.16) and (3.19) with the following boundary conditions for the phase-field model of hardening concrete are obtained.

$$\mathbf{u} = \bar{\mathbf{u}} \quad \text{on} \quad \partial\mathcal{B}_u \quad (3.21)$$

$$\boldsymbol{\sigma}\mathbf{n} = \bar{\mathbf{t}} \quad \text{on} \quad \partial\mathcal{B}_t \quad (3.22)$$

$$\partial_{\nabla d}\gamma_l \cdot \mathbf{n}_{\mathcal{L}} = 0 \quad \text{on} \quad \partial\mathcal{L} \quad (3.23)$$

3.3 Stress Response

We employ the so-called hybrid formulation, see Ambati, Gerasimov, and De Lorenzis [43]. Therefore, the stress response can be expressed using degradation function as

$$\boldsymbol{\sigma} = \hat{\boldsymbol{\sigma}}(\boldsymbol{\varepsilon}, d, \xi) = \hat{g}(d)\hat{\boldsymbol{\sigma}}_0(\boldsymbol{\varepsilon}, \xi) \quad (3.24)$$

where $\hat{g}(d)$ is defined as

$$\hat{g}(d) := (1 - d)^2. \quad (3.25)$$

The degradation function expresses the degradation of the stress tensor and fulfill the conditions

$$g(0) = 1, \quad g(1) = 0, \quad g'(1) = 0. \quad (3.26)$$

The first two conditions represent the unbroken and fully broken cases, respectively. The last one is for ensuring the convergence of energetic fracture force if the damage converges to fully broken state.

The rigidity of concrete increases as it undergoes hydration during the hardening process, which leads to changes in its elastic constants, e.g., the Lamé constant and the shear modulus, over time. This fact leads to an approach of the incremental stress update, such that

$$\hat{\boldsymbol{\sigma}}_0 = \hat{\boldsymbol{\sigma}}_{0n} + \mathbb{C} : \Delta\boldsymbol{\varepsilon}_{n+1}^e, \quad (3.27)$$

where $\hat{\boldsymbol{\sigma}}_{0n}$ is the non-degraded stress tensor at time t_n and $\Delta\boldsymbol{\varepsilon}_{n+1}^e$ is the incremental elastic strain tensor for the time step of $[t_n, t_{n+1}]$. Moreover, \mathbb{C} are the current tangent moduli, expressed as

$$\mathbb{C} = \hat{\lambda}(\chi)\mathbf{1} \otimes \mathbf{1} + 2\hat{\mu}(\chi)\mathbb{I}. \quad (3.28)$$

The hydration-dependent elastic parameters $\hat{\lambda}(\chi)$ and $\hat{\mu}(\chi)$ are, respectively, the Lamé constant and the shear modulus, which are the functions of the aging degree, χ , that is going to be introduced in (3.49), and they should conform with the conditions of $\hat{\lambda}(\chi) > 0, \hat{\mu}(\chi) > 0$. Also, $\mathbf{1}$ and \mathbb{I} represent the second-order identity tensor and the fourth-order identity tensor, respectively.

The elastic part of the strain tensor, $\boldsymbol{\varepsilon}^e$, is defined as the difference between the total strain tensor and the shrinkage strain tensor, $\boldsymbol{\varepsilon}^{sh} := \varepsilon^{sh} \mathbf{1}$, as

$$\boldsymbol{\varepsilon}^e = \boldsymbol{\varepsilon} - \boldsymbol{\varepsilon}^{sh}. \quad (3.29)$$

3.4 Crack Driving Force

Miehe et al. [44] identified the crack driving force with the crack driving state function, \tilde{D} , which depends on set state of state variables. The crack driving force can be stated as

$$\mathcal{H}_d = \frac{G_c}{2l} \max_{s \in [0, t]} (\tilde{D}(\text{State}(\mathbf{x}, s)), \mathcal{H}_n). \quad (3.30)$$

The crack driving state function, based on the energy-based approach,

$$\tilde{D} = \zeta \left\langle \frac{\psi_0^+}{\psi_c} - 1 \right\rangle \quad (3.31)$$

is formulated in terms of the positive part of the energy storage function with a energy storage function threshold, ψ_c . Hydration products are created as concrete hardens through the hydration process. As the hydration products continue to form and mature over time, the concrete becomes more rigid and its material parameters change. This process also leads to the development of an incremental update of the positive part of the energy storage function, as mentioned in (3.30). Therefore, the current value of the positive part of the energy storage function is defined as

$$\psi_{0n+1}^+(\boldsymbol{\varepsilon}) = \psi_{0n}^+(\boldsymbol{\varepsilon}) + \Delta\psi_0^+(\boldsymbol{\varepsilon}), \quad (3.32)$$

where $\Delta\psi_0^+(\boldsymbol{\varepsilon})$ is the increment of energy storage function and it is expressed by

$$\Delta\psi_0^+(\boldsymbol{\varepsilon}) = \boldsymbol{\sigma}_0^+ : \Delta\boldsymbol{\varepsilon}_+^e. \quad (3.33)$$

The incremental elastic strain tensor, $\Delta\boldsymbol{\varepsilon}_\pm^e$, in (3.33) is defined by

$$\Delta\boldsymbol{\varepsilon}_\pm^e := \boldsymbol{\varepsilon}_\pm^e - \boldsymbol{\varepsilon}_{n\pm}^e, \quad (3.34)$$

where the positive and negative parts of the elastic strain tensor are defined by using the Macaulay brackets as

$$\boldsymbol{\varepsilon}_{\pm}^e := \sum_{i=1}^{\delta} \langle \varepsilon_i \rangle_{\pm} \mathbf{n}_i \otimes \mathbf{n}_i, \quad (3.35)$$

where $\varepsilon_{1,\dots,\delta}$ are the principal elastic strains and the $\mathbf{n}_{1,\dots,\delta}$ are the principal directions.

The positive part of the non-degraded stress tensor, $\boldsymbol{\sigma}_0^+$, in (3.33) is defined as

$$\boldsymbol{\sigma}_0^+ = \boldsymbol{\sigma}_{0n}^+ + \Delta \boldsymbol{\sigma}_0^+ \quad (3.36)$$

and the positive part of the incremental non-degraded tensile stress tensor is calculated as

$$\Delta \boldsymbol{\sigma}_0^+ = \mathbb{C} : \Delta \boldsymbol{\varepsilon}_+^e. \quad (3.37)$$

3.5 Hydration of Cement

Concrete gains its strength and rigidity through highly exothermic reaction that is called hydration. The degree of hydration, ξ , is introduced as the measure of the extent of hydration, [45], [46], [42]. Its definition can be made as the ratio of amount of heat liberated per unit volume to the final amount of liberated heat per volume under ideal conditions. Thus, it is expected that the degree of hydration should reach 1 for complete hydration.

The evolution of the degree of hydration is adopted from the work of Di Luzio and Cusatis [42] and is described as

$$\dot{\xi} = \tilde{A}_{\xi}(\xi) \beta(h) \exp\left(-\frac{E_{ac}}{RT}\right), \quad (3.38)$$

where $\tilde{A}_{\xi}(\xi)$ is defined as the normalized affinity that completely characterizes the hydration kinetics and it is stated as

$$\tilde{A}_{\xi} = A_{c1} \exp\left(-\frac{\eta \xi}{\xi^{\infty}}\right) \left(\frac{A_{c2}}{\xi^{\infty}} + \xi\right) (\xi^{\infty} - \xi), \quad (3.39)$$

E_{ac} is activation energy for hydration; R is the universal constant for ideal gases with the value of 8.315 J/(mol K); η , A_{c1} , and A_{c2} are the material parameters.

The factor $\beta(h)$ appearing in the (3.38) is related with moisture effects on the hydration and it is expressed as

$$\beta(h) = [1 + (5.5 - 5.5h)^4]^{-1}, \quad (3.40)$$

where h is referred to as the moisture. In the scope of this work, moisture effects are not considered and thus we take h as 1. For $h = 1$, $\beta(h)$ becomes 1 and (3.38) yields to the one that Cervera et al. [46] have defined. However, the parameter values related with the normalized affinity, (3.39), used in this work are validated and calibrated using the one that Di Luzio and Cusatis [42] described. Thus, for the sake of convenience evolution of the degree of hydration (3.38) defined by Di Luzio and Cusatis [42] is used.

The Newton-Raphson scheme is adopted for the iterative update of ξ through the non-linear evolution equation,

$$\xi_{k+1} = \xi_k - a_k^{-1} r_k, \quad (3.41)$$

where r is referred as residual and could be calculated as

$$r_k = \xi_{k+1} - \xi_k - (t_{n+1} - t_n) \dot{\xi}_{n+1}. \quad (3.42)$$

Also, a is defined as

$$a = \frac{dr}{d\xi}. \quad (3.43)$$

3.6 Aging Mechanism

The hardening of mortar is characterized by hydration. Concrete gains its rigidity and strength over time during the hardening process. Thus, the material properties of young concrete change over time during hardening. Cervera et al. [46] introduce an intermediate variable called the degree of aging for the relation of the hydration degree with the aging of concrete [46]. Mechanical properties including the compressive strength $f_c(\chi)$, the tensile strength $f_t(\chi)$, and the elastic modulus $E_c(\chi)$ are defined as

$$f_c(\chi) = \chi f_\infty \quad (3.44)$$

$$f_t(\chi) = 0.1 f_c(\chi) \quad (3.45)$$

$$E_c(\chi) = \chi^{2/3} E_\infty, \quad (3.46)$$

where E_∞ is the final value of the elastic modulus and f_∞ denotes the final compressive strength of concrete corresponding to the fully hydrated state.

Then, the Lamé constants introduced in 3.28 can be calculated using the elastic modulus and the Poisson's ratio by

$$\hat{\lambda}(\chi) = \frac{E_c(\chi)\nu}{(1-\nu)(1-2\nu)}, \quad (3.47)$$

$$\hat{\mu}(\chi) = \frac{E_c(\chi)}{2(1+\nu)}. \quad (3.48)$$

The degree of aging definition is adopted from the work of Di Luzio and Cusatis [42] where it is given by

$$\dot{\chi} = \dot{\xi} \left(\frac{T_{max} - T}{T_{max} - T_{ref}} \right)^{\eta_\chi} (B_\chi - 2A_\chi\xi) \quad (3.49)$$

with the conditions of $\xi > \xi_0$, otherwise $\dot{\chi} = 0$. ξ_0 is the value of the degree of hydration at the end of the setting phase, in which concrete could be regarded as solid. T_{max} is the maximum temperature that hardening can take place, T_{ref} is the reference temperature that the calibration of model is done. In this work T is taken as constant. Therefore, we have

$$\frac{T_{max} - T}{T_{max} - T_{ref}} = 1. \quad (3.50)$$

Moreover, η_χ and A_χ , appearing in (3.49) are the model parameters that should be identified based on the experimental data. Also, B_χ is defined as

$$B_\chi = \frac{1 + A_\chi(\xi_\infty^2 - \xi_0^2)}{\xi_\infty - \xi_0}. \quad (3.51)$$

CHAPTER 4

NUMERICAL EXAMPLES

The numerical examples are presented to investigate the development of residual stresses, due to hardening, in terms of principal stresses and the evolution of the ratio of principal stresses to the instantaneous tensile strengths, β , and consequently investigate the effect of residual stresses on the hardened meso-structure using brittle phase-field fracture analyses. In the light of the governing and constitutive equations introduced in Chapter 3, numerical examples are conducted using the Finite Element Analysis Program (FEAP) [47]. The mesh that are used in the following numerical examples are generated using the Computational Geometry Algorithms Library (CGAL) [48].

This chapter is divided into three parts, the validation of the numerical solutions, the development of residual stresses due to hardening of mortar, and the fracture behavior of meso-structure in tension. The validation of the methodology is conducted in Section 4.1 through the comparison of the analytical and the numerical solutions of a model of pure mortar sample in Section 4.1.1, the investigation of mesh convergence in Section 4.1.2, and the statistical study in Section 4.1.3. In Section 4.2, the development of residual stresses is investigated by considering different cases. With this objective, different meso-structure models are generated according to Chapter 2. Different cases are numbered with Roman numerals I to VII. Case I, the control case, is used as a point of comparison for the other cases. In Section 4.2.1 the total area fraction of coarse aggregates, in Section 4.2.2 the assessment of segregation effect which may occur due to over vibration of fresh concrete, the effect of elongation ratio in Section 4.2.3, and the effect of the shape of aggregates in Section 4.2.4 are examined in terms of the development of principal stresses and the evolution of the ratio of principal stresses to the instantaneous tensile strengths, β . The examinations are con-

ducted through the comparisons at the end of four different times, 1. Day, 7. Day, 14. Day, and 28. Day. All cases related with each section are presented in Table 4.4. The applied shrinkage strain is given in Figure 4.3. The dimensions of all meso-structures are $150 \text{ mm} \times 150 \text{ mm}$.

In Section 4.2 the effect of residual stresses on the tensile behavior of hardened meso-structure is examined, also the cases given in Table 4.4 are compared under tensile loading in the presence and absence of residual stresses.

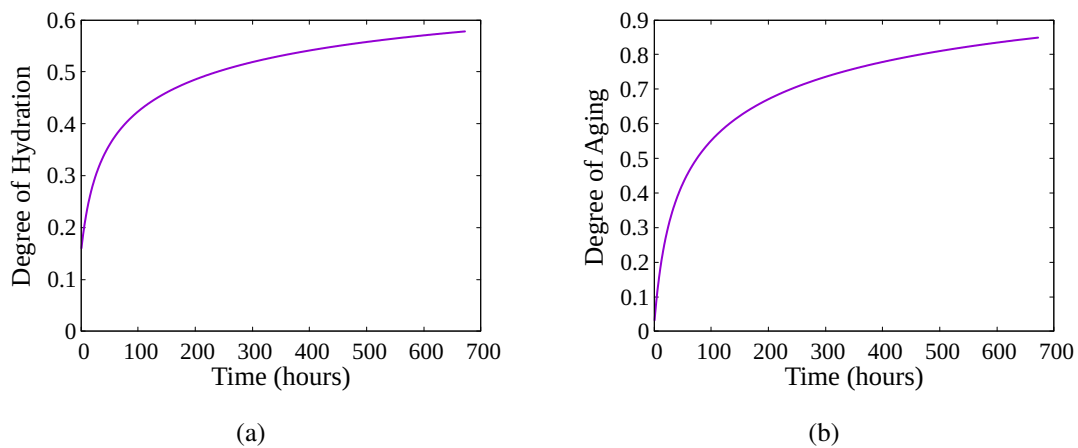


Figure 4.1: (a) Evolution of degree of hydration (b) Evolution of degree of aging

In the following numerical analyses, the hardening of concrete for 28 days is considered. The evolution of the degree of hydration according to hydration kinetics presented in Section 3.5 and the evolution of the degree of aging described in Section 3.6 are shown in Figure 4.1. Analyses using different evolutions of the degree of hydration, Figure 4.2, are conducted and they are resulted in close values of maximum principal stresses, Table 4.1. Therefore, for the sake of convenience the evolution presented in Figure 4.1a is used.

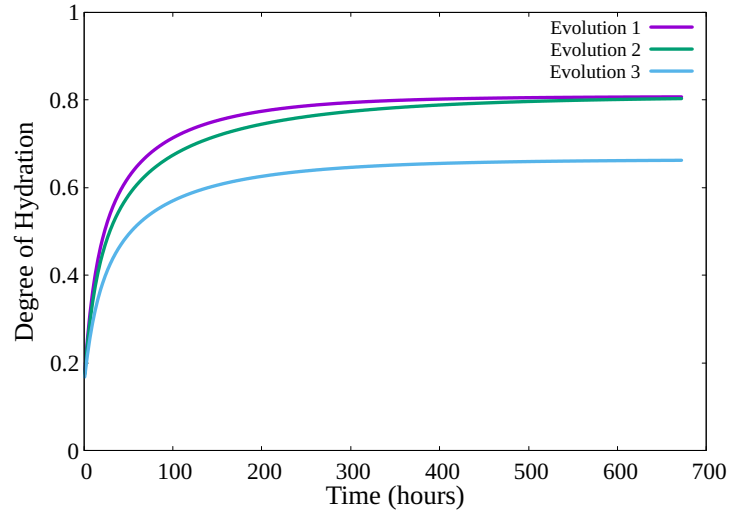


Figure 4.2: The degree of hydration with respect to time

Table 4.1: Maximum principal stresses ($\text{MPa} \times 10^{-2}$)

Evolution 1	Evolution 2	Evolution 3
5.94	5.89	4.31

The material parameters that are used for all presented numerical examples are given in Table 4.2, the modulus of elasticity value given for the mortar represents the value when the degree of aging reaches to 1. The Poisson's ratio of mortar remains constant throughout the hydration and other parameters related with the degree of hydration are given in Table 4.3.

Table 4.2: Material Parameters

Constituents	Modulus of Elasticity (GPa)	Poisson's ratio
Mortar	20	0.18
Aggregates	40	0.18

Table 4.3: Parameters governing the hydration of mortar

Parameter	Units	Value
A_{c1}	h^{-1}	6×10^7
A_{c2}	-	7×10^{-3}
η	-	6.5
w/c	-	0.66
E_{ac}	J mol^{-1}	45646
R	$\text{J}/(\text{mol K})$	8.315

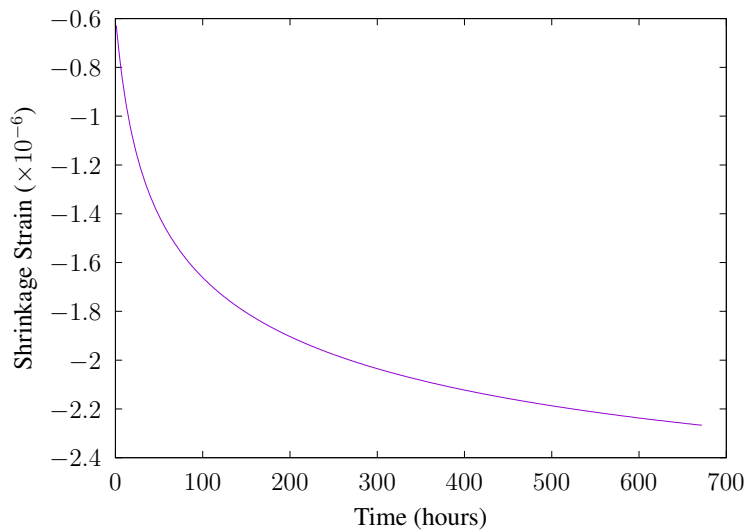
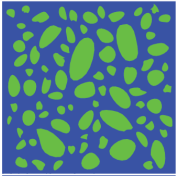
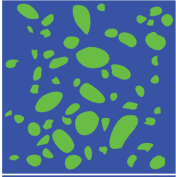
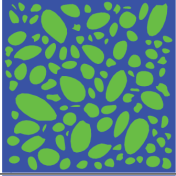
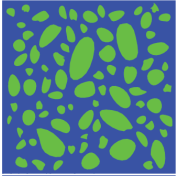
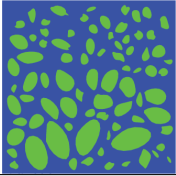
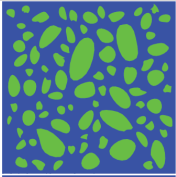
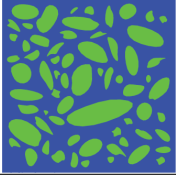
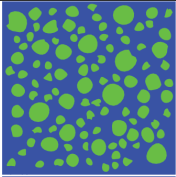
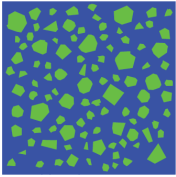


Figure 4.3: Applied Shrinkage Strains

Table 4.4: Numerical example cases

Related Section	Case	Examined parameter	Area ratio	Elongation	Figure
Section 4.2.1	Case I	Control Case	0.5	1 ~ 2	
	Case II	Area Ratio	0.35	1 ~ 2	
	Case III	Area Ratio	0.6	1 ~ 2	
Section 4.2.2	Case I	Control Case	0.5	1 ~ 2	
	Case IV	Segregation	0.5	1 ~ 2	
Section 4.2.3	Case I	Control Case	0.5	1 ~ 2	
	Case V	Elongation	0.5	1 ~ 3	
Section 4.2.3	Case VI	Round Edges	0.5	1 ~ 2	
	Case VII	Sharp Edges	0.5	1 ~ 2	

4.1 Validations

Validations of the conducted numerical solutions are presented in this section. Comparison of analytical and numerical solutions for the stress evolution in a hardening of mortar is presented in Section 4.1.1, the mesh convergence study is carried out in Section 4.1.2, and the linear elastic calculations to verify the statistical representativeness of fifty meso-structures generated for Case I are conducted in Section 4.1.3.

4.1.1 Hardening of Mortar

In this example, stress evolution in a hardening of mortar is investigated. To ensure that the numerical implementation in this work is done correctly the comparison of analytical solution and the solution obtained from the implementation are compared. For this purpose, material point analyses with uniform strain field are performed. In these plain-strain analyses, the normal strain in the vertical direction and the normal stress in the horizontal direction are set to zero.

4.1.1.1 Analytical Solution

The evolution of material parameters necessitates an incremental update of the stress tensor, as it is described in (3.27). Since the loading is only applied as shrinkage, the occurrence of any mechanical strain is not expected except for the one in the direction of x . The elastic strain tensor can be obtained as defined at (3.29), such that

$$\begin{aligned}\boldsymbol{\varepsilon}^e &= \boldsymbol{\varepsilon} - \varepsilon^{sh} \mathbf{1} \\ \boldsymbol{\varepsilon}^e &= \begin{bmatrix} \varepsilon_{11} & 0 & 0 \\ 0 & 0 & 0 \\ 0 & 0 & 0 \end{bmatrix} - \varepsilon^{sh} \begin{bmatrix} 1 & 0 & 0 \\ 0 & 1 & 0 \\ 0 & 0 & 1 \end{bmatrix} \\ &= \begin{bmatrix} \varepsilon_{11} - \varepsilon^{sh} & 0 & 0 \\ 0 & -\varepsilon^{sh} & 0 \\ 0 & 0 & -\varepsilon^{sh} \end{bmatrix}.\end{aligned}$$

Subtracting the forms of two consecutive time step of the algorithmic form of (3.29),

$$\Delta\boldsymbol{\varepsilon}^e = \Delta\boldsymbol{\varepsilon} - \Delta\varepsilon^{sh}\mathbf{1}, \quad (4.1)$$

incremental elastic strain tensor can be obtained. Since there are no restraints in the x direction, the stress and thus the incremental stress in that direction will not exist, i.e.

$$\Delta\sigma_{11} = 0. \quad (4.2)$$

Utilizing the input of Lamé parameter values, along with the incremental stress formulation presented in (3.27) and the condition outlined in (4.2), ε_{11} can be obtained as

$$\Delta\sigma_{11} = \mathbb{C}_{11kl} : \Delta\varepsilon_{kl} = 0 \quad (4.3)$$

The elastic strain is obtained using the value of ε_{11} . Therefore, by using (3.27), σ_{22} can be calculated and compared to the findings obtained from the finite element solution with the boundary conditions leading to the same strain state. The comparison of the maximum principal stresses obtained from the material point (driver) calculations with those from the finite element analysis in Figure 4.4 indicates that the numerically obtained shrinkage-induced principal stress values agree well with the analytically obtained results.

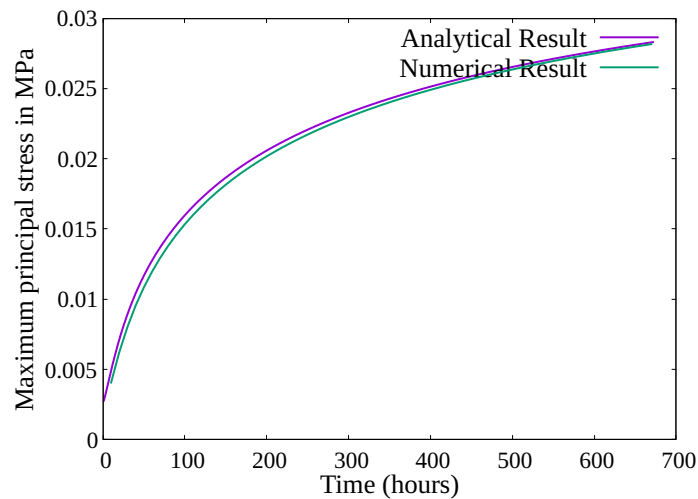


Figure 4.4: Analytical and numerical results

4.1.2 Mesh Convergence

The mesh convergence study of a hardened specimen and a hardening specimen is conducted in this section for different values of mesh sizes. The analyses are conducted using triangular finite elements with maximum edge lengths of 0.3 mm, 0.5 mm, 1.0 mm, 1.5 mm, 2.0 mm, 3.0 mm, and 4.0 mm. For this purpose, both three-node and six-node triangles are used and it is observed that three-node triangles having 0.5 mm maximum edge length result in sufficiently accurate results.

4.1.2.1 Hardened Specimen

The finite element analyses of the meso-structure of Case I (Table 4.4) for the hardened concrete with the material parameters given in Table 4.2 are conducted using three-node triangles and six-node triangles. Maximum lengths of a triangle edge are 0.3 mm, 0.5 mm, 1.5 mm, 2 mm, 3 mm, and 4 mm. Upper and lower edge of the section are restrained in both x and y directions. Time step is taken as 0.001 and the total step number is 100, displacement is applied proportional to the time with the range of $0 - 0.01 \times 150$ mm at $y = 150$ mm in the direction of y . The convergence of the mesh could be observed with the Figure 4.5.

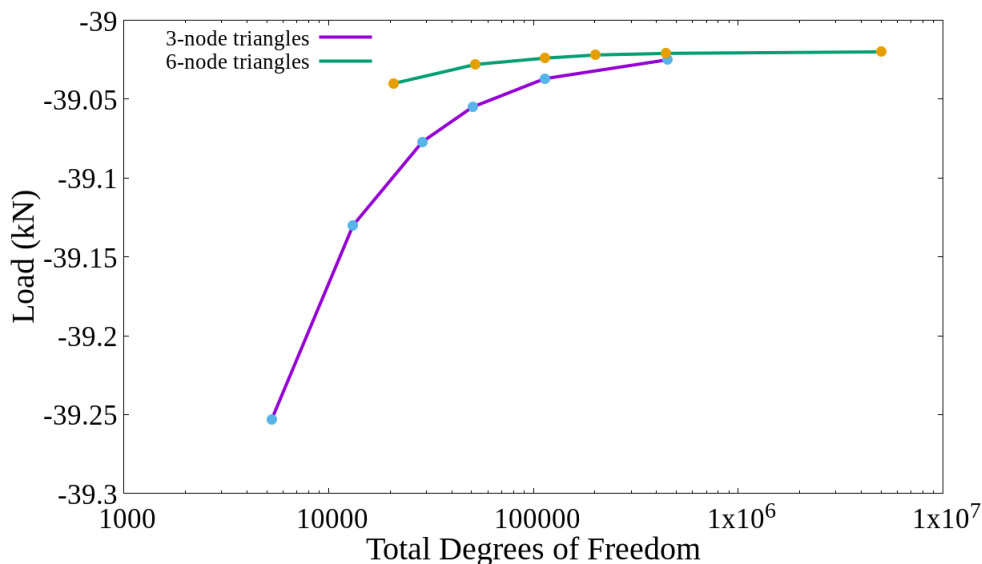


Figure 4.5: Reaction loads with respect to total degrees of freedom

4.1.2.2 Hardening Specimen

The geometry of models are the same as the one described in Section 4.1.2.1. At the lower edge of the section translation in y direction is restrained. There is no mechanical loading, only the shrinkage is applied while mortar is hardening. The analyses are carried out with meshes that have the maximum edge lengths of 0.3 mm, 0.5 mm, 1 mm, 1.5 mm, 2 mm, 3 mm, and 4 mm. Material parameters are given in Tables 4.2 and 4.3, the elastic modulus given for the mortar is the value at the end of the hardening process. The displacement values for the nodes that are placed at the left and right upper edge of the section are given in Table 4.5. The convergence of the analyses can be observed in Figure 4.6 where x axis represents the total degrees of freedom of related mesh and the y axis represents the displacement of upper rightmost node of related mesh in y direction, which is also given in Table 4.5. The convergence analyses conducted on both hardened and hardening specimen indicate that three-node linear triangular elements with edge length smaller than 1 mm and six-node quadratic triangular elements with edge length smaller than 2 mm give sufficiently accurate results. In this study, we use three-node triangles with edge of length 0.5 mm in the residual stress calculations in Section 4.2 and three-node triangles with edge of length 1 mm in the fracture analyses in Section 4.3 for the sake of convenience.

Table 4.5: Displacement values ($\text{mm} \times 10^{-4}$) in y direction of nodes at left and right upper edge

Maximum Edge Length mm	3-Node		6-Node	
	Left Node	Right Node	Left Node	Right Node
$h_{max} = 4.0$	-2.1983	-2.0195	-2.2289	-2.0508
$h_{max} = 3.0$	-2.2128	-2.0382	-2.2309	-2.0529
$h_{max} = 2.0$	-2.2214	-2.0470	-2.2316	-2.0534
$h_{max} = 1.5$	-2.2256	-2.0497	-2.2318	-2.0536
$h_{max} = 1.0$	-2.2289	-2.0519	-2.2320	-2.0537
$h_{max} = 0.5$	-2.2312	-2.0532	-2.2321	-2.0537
$h_{max} = 0.3$	-2.2318	-2.0535	-2.2321	-2.0537

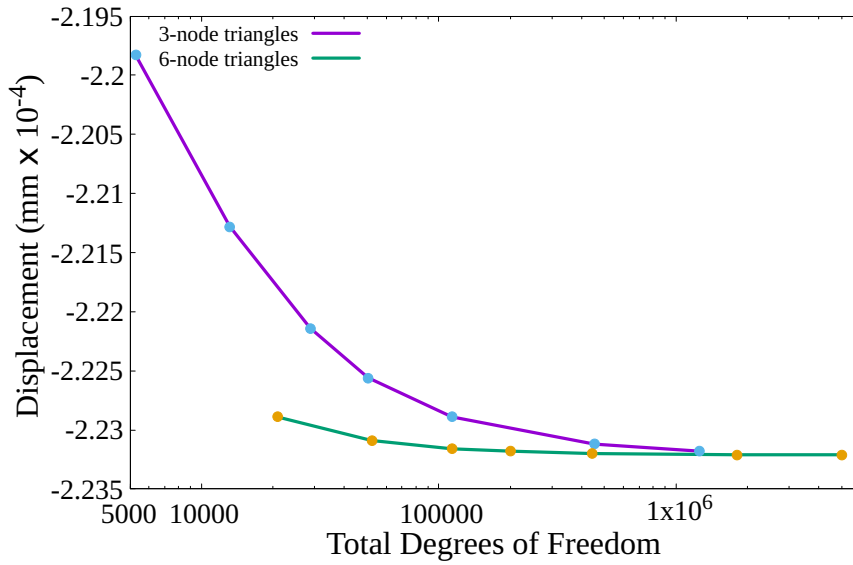
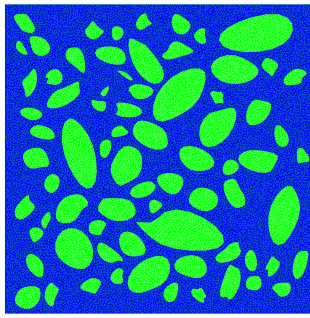


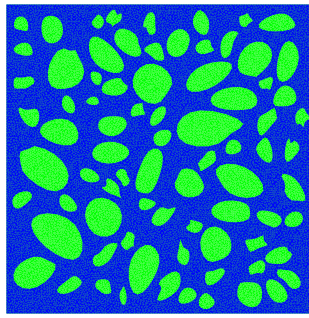
Figure 4.6: Displacement in y direction of upper leftmost node with respect to total degrees of freedom

4.1.3 Statistical Study

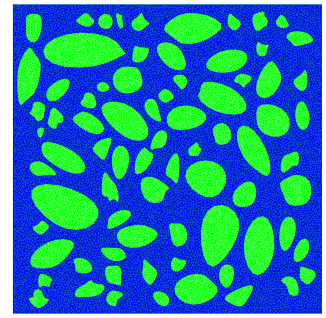
In this section, the deviation of maximum principal stress and stiffness values obtained from meso-structures having the same set of parameters, referred as subcases, is examined. With this objective, 50 subcases with the cross-section of $150 \times 150 \text{ mm}^2$ are obtained using control parameters and 9 of them are depicted in Figure 4.7. The geometry, the material parameters, and the loading are exactly the same given in Section 4.1.2. In the analyses, three-node triangles are used with the maximum edge length of 0.5 mm. At the upper and lower edge of the section translation in y direction is restrained, at the leftmost nodes at both upper and lower edge the translation in x direction is also restrained. The maximum principal stress attained for all subcases is given in Figure 4.9. The load displacement curves for every subcase is given in Figure 4.8 and the stiffness values are shown in Figure 4.10. The distribution of principal stresses and stiffness values with respect to the total subcase numbers are shown in Figures 4.11 and 4.12.



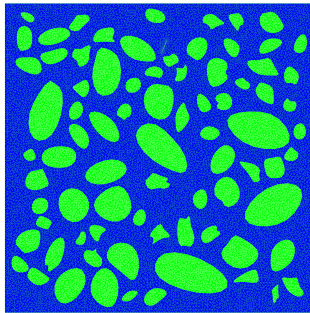
(a) Subcase 1



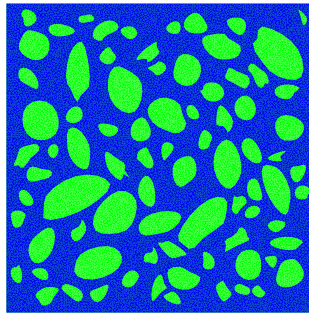
(b) Subcase 2



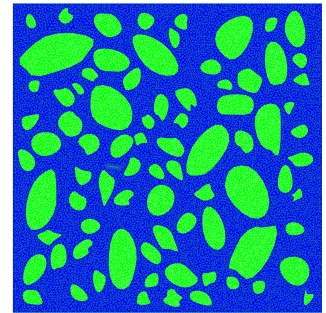
(c) Subcase 3



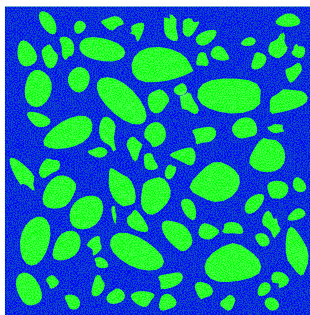
(d) Subcase 4



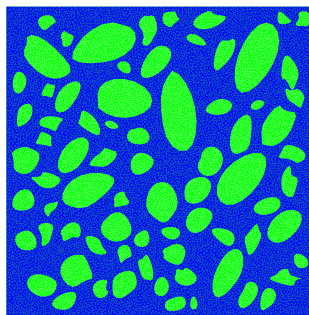
(e) Subcase 5



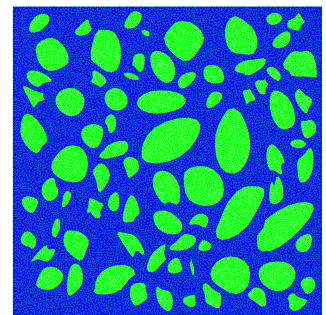
(f) Subcase 6



(g) Subcase 7



(h) Subcase 8



(i) Subcase 9

Figure 4.7: Nine examples of subcases obtained with control parameters

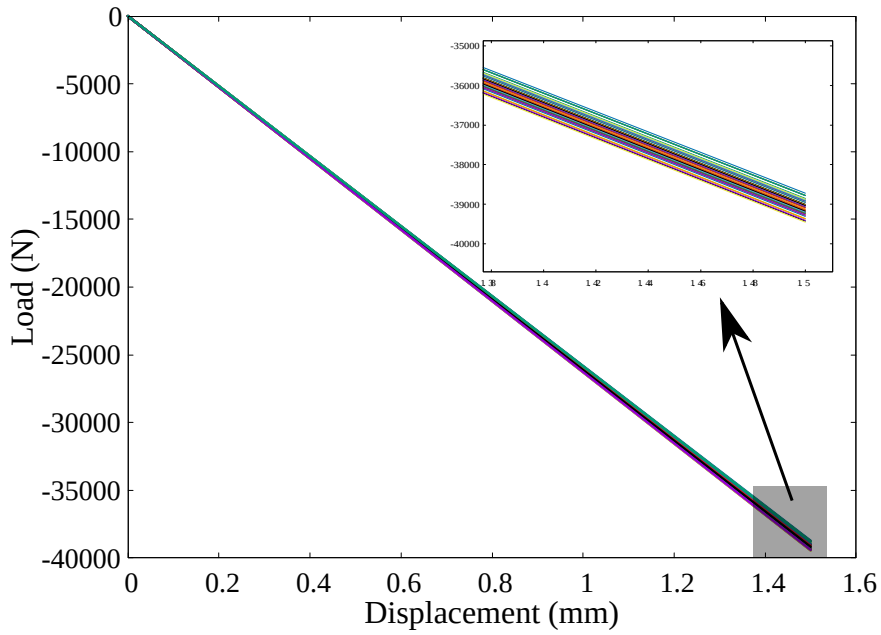


Figure 4.8: Load-displacement at $y = 150$ mm in y direction

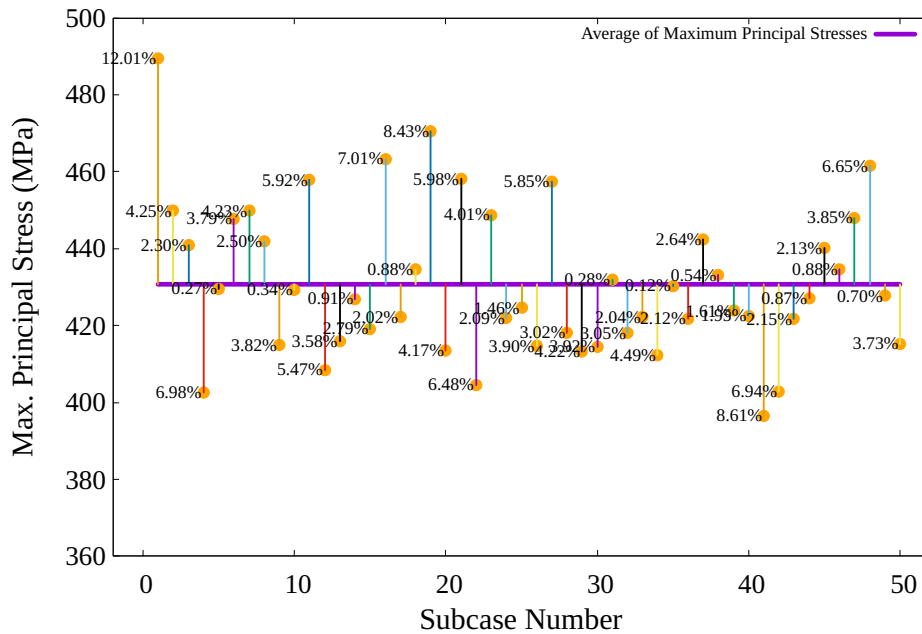


Figure 4.9: Maximum principal stress of each subcase and its deviation from the average value

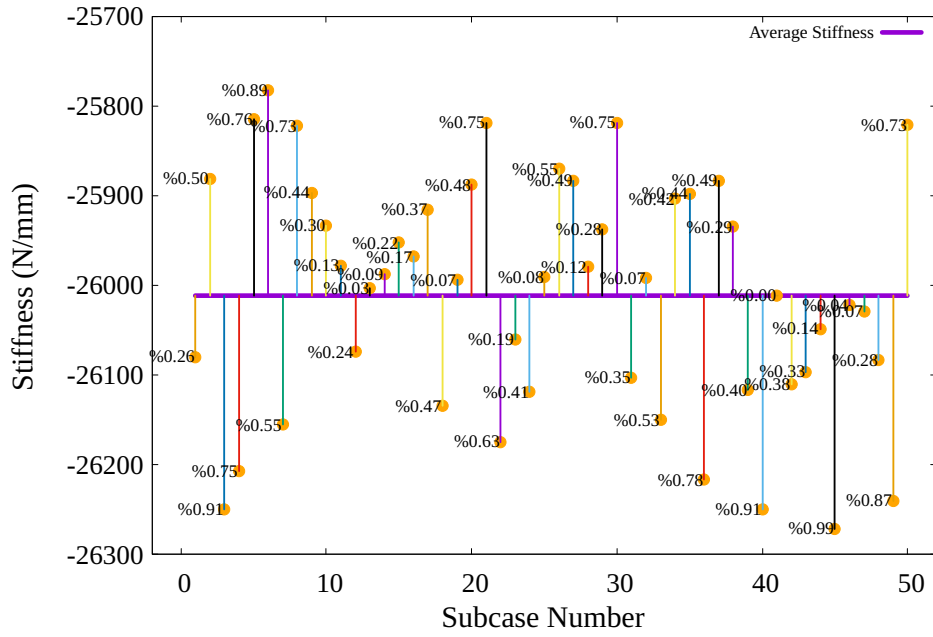


Figure 4.10: Stiffness values of each subcase and its deviation from the average value

The statistical analysis conducted through the generation of fifty subcases of the control case (Case I in Table 4.4) indicate that the dispersion of the stiffness value among the subcases is quite small as shown in Figures 4.8, 4.10, and 4.12. The maximum deviation from the average stiffness is less than 1%, see Figure 4.10. Although the variation of the maximum principal stress among subcases is overall less than 9%, this value falls into the nearly 6% for majority of cases as shown in Figure 4.9, see also Figure 4.11. Based on these results obtained from the statistical analysis conducted on Case I (Control), we conclude that one meso-structure randomly generated for each of seven different cases, presented in Table 4.4, is sufficiently representative for the investigations presented in Sections 4.2 and 4.3.

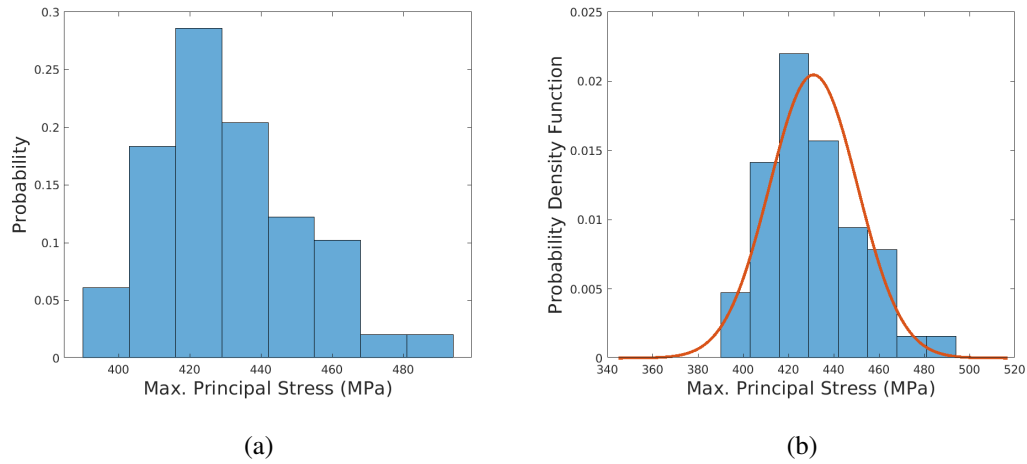


Figure 4.11: Density and probability density distribution functions of principal stresses

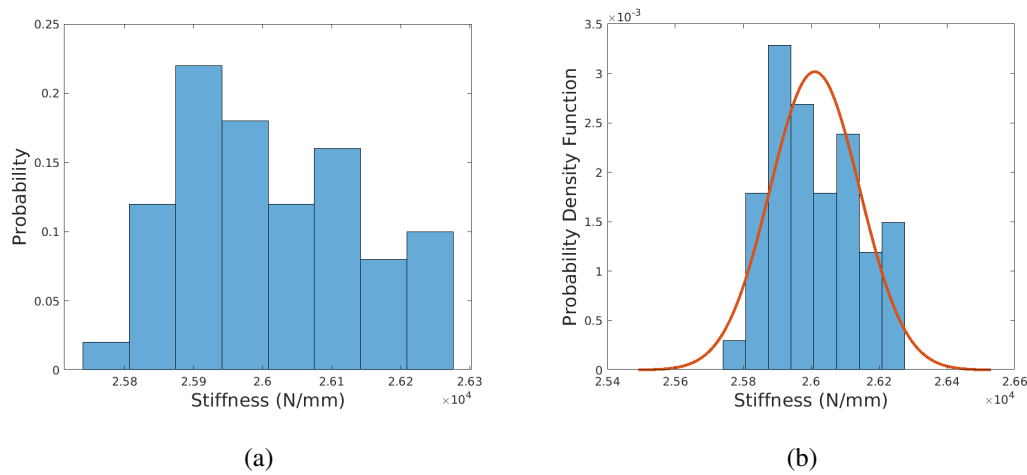


Figure 4.12: Density and probability density distribution functions of stiffness values

4.2 Shrinkage-Induced Residual Stress Evolution

The investigation of the evolution of the residual stresses for hardening mortar under autogenous shrinkage is conducted in this section. The evolution of the crack phase-field is deactivated during the residual stress analysis. The translation in y direction of bottom-edge nodes are fixed and springs that are active only in compression are

placed at the left-edge and the right-edge nodes of the meso-structure as it is shown in Figure 4.13. Furthermore, the nodes at the top-edge free to move in both directions. The comparison between the cases is made in terms of the maximum principal stress values and the values of β , which is defined as the instantaneous ratio of the maximum principal stress to the tensile strength.

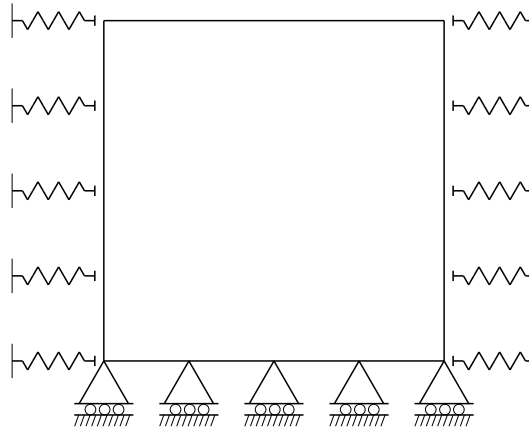


Figure 4.13: Boundary Conditions

4.2.1 Area Ratio

The area ratio refers to the ratio of area of aggregates to the cross-sectional area of the cross-section as stated in Wang et al. [22]. Case II and Case III are inspected and compared with the control case (Case I). The duration of the analysis is 28 days. The area ratio of Case I is 0.5. At the end of 28 days, the maximum principal stress obtained is 0.036 MPa and the maximum β ratio is 0.01. The area ratio of Case II is 0.35. At the end of 28 days, the maximum principal stress obtained is 0.035 MPa and the maximum β ratio is 0.0098. The area ratio of Case III is 0.6. At the end of 28 days, the maximum principal stress obtained is 0.034 MPa and the maximum β ratio is 0.0090. The principal stress and β values are shown for the compared cases in Figures 4.14(a) and 4.15(a). For every case the maximum principal stress and β values are shown for different days to be able to observe the evolutions of them. The days are selected to be 1, 7, 14, and 28. Each row of the Figures 4.14(a) and 4.15(a) represents the case stated at the far left of the row and each column represents the the end of the day from which the values are taken, for every column corresponding

legend is given at the base of the column.

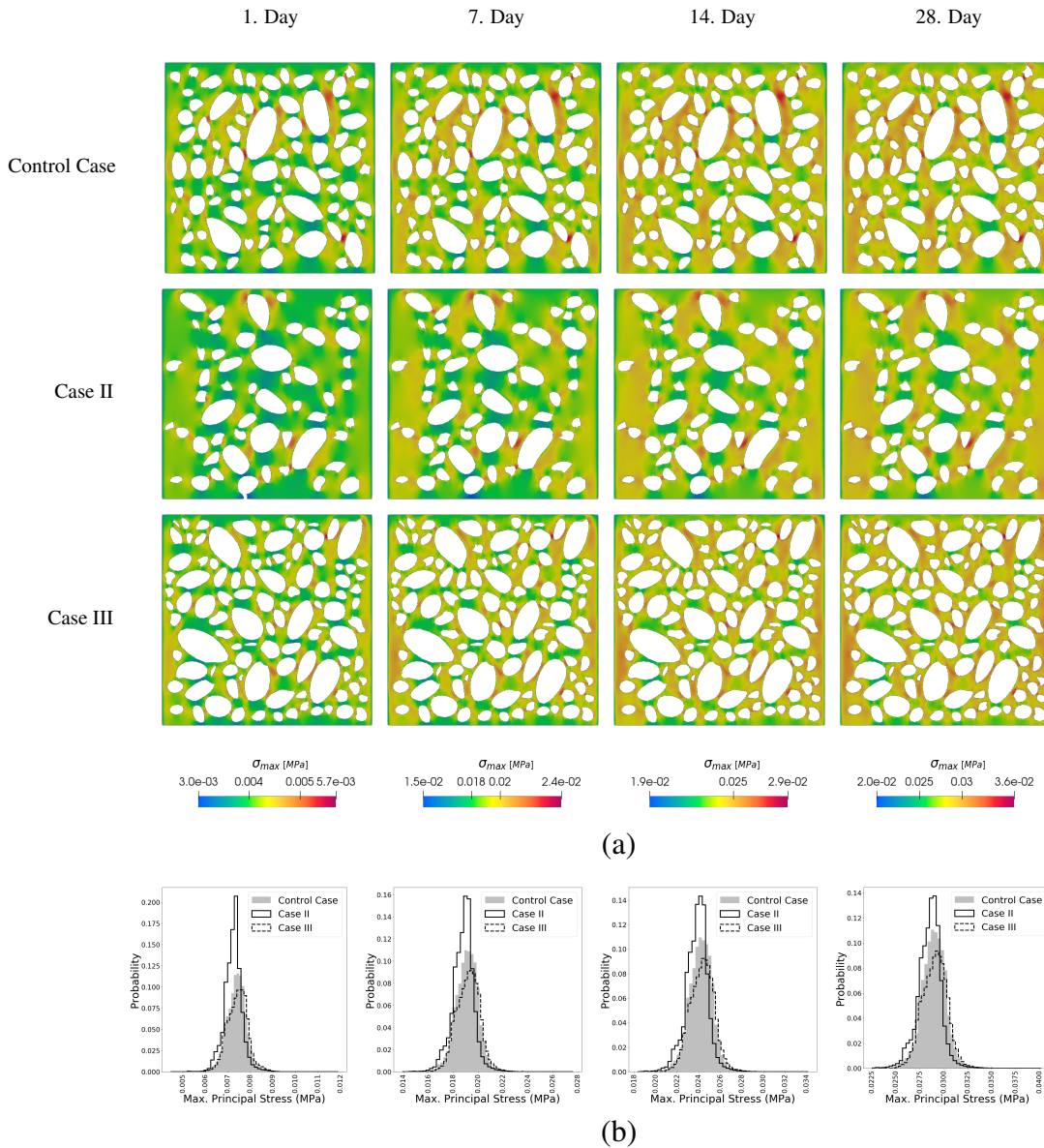


Figure 4.14: Maximum principal stress values (a) Contour plots (b) Histograms

Histogram plots are utilized to compare the cases. The plots are given in Figures 4.14(b) and 4.15(b) for principal stresses and β values respectively. The columns in Figures 4.14(a) and 4.15(a) are aligned with corresponding histogram plots of Figures 4.14(b) and 4.15(b). In Figure 4.14(b) Case II has a higher probability of having lower values of maximum principal stresses and Case III has a higher probability of having higher values of maximum principal stresses. The reason behind the histogram plots of Case III and Control Case are not much distinct from each other that the area ratio

interval between Control Case and Case II is higher than the interval between Control Case and Case III, another reason can be that the increase in probability can have a non-linear relation with the area ratio of the meso-structure. Therefore, the observation of an increasing probability of maximum principal stresses with increasing area ratio of the meso-structure can be made.

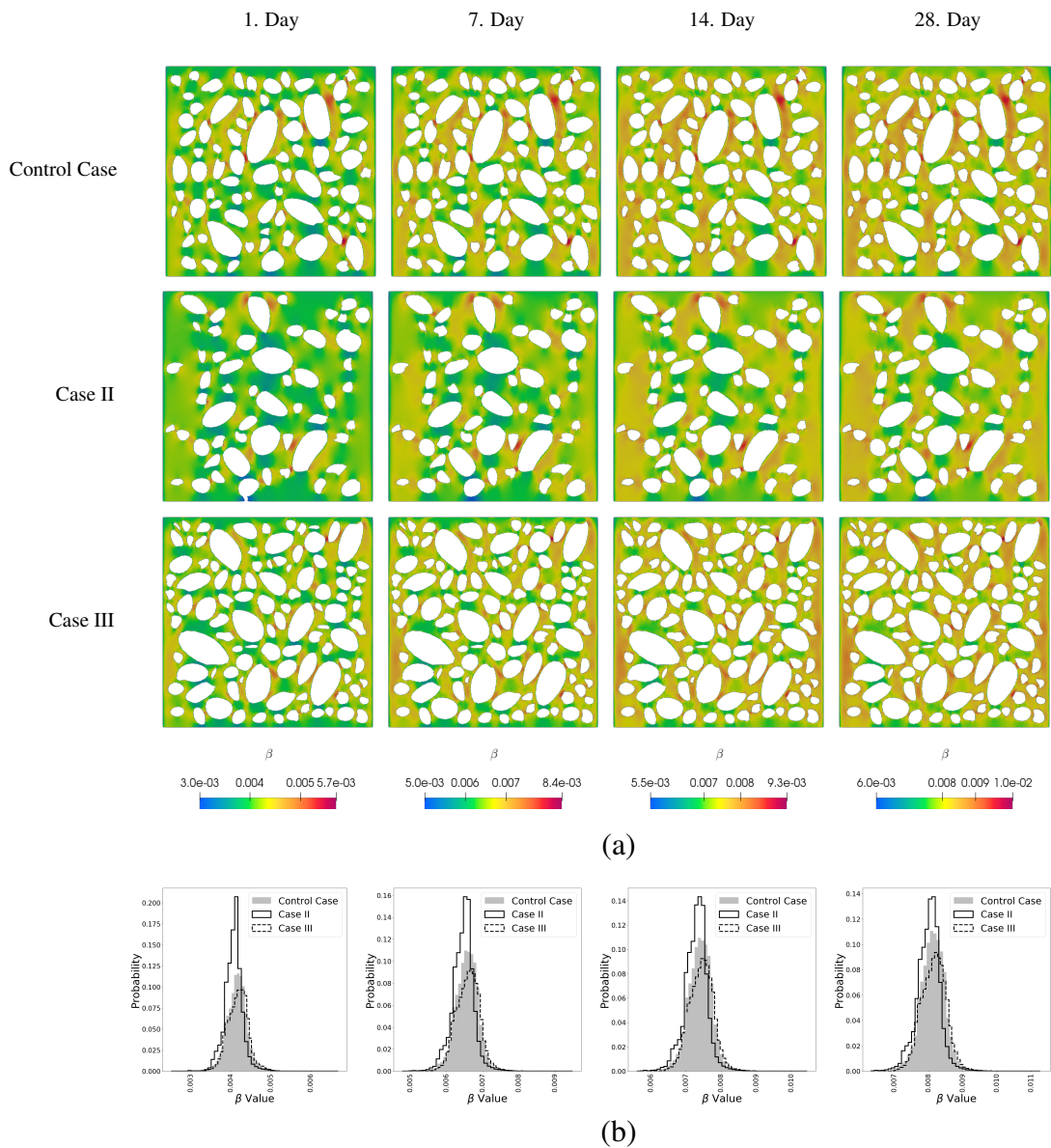


Figure 4.15: β values (a) Contour plots (b) Histograms

4.2.2 Segregation

Segregation can be defined as the separation of some size of aggregates from the mortar. It is mainly due to the over vibration of fresh concrete. It can result in honeycombing, a decrease in ultimate strength. All parameters of Case IV are the same with that of the control case. Only the placing process of the aggregate is manipulated to obtain a segregated model where coarser aggregates appear denser in the lower part of the section. At the end of 28 days, the maximum principal stress obtained is 0.035 MPa and the maximum β ratio is 0.0097. The principal stress and β values are shown for the compared cases in Figures 4.16(a) and 4.17(a). For every case the maximum principal stress and β values are shown for different days to be able to observe the evolutions of them. The days are selected to be 1, 7, 14, and 28.

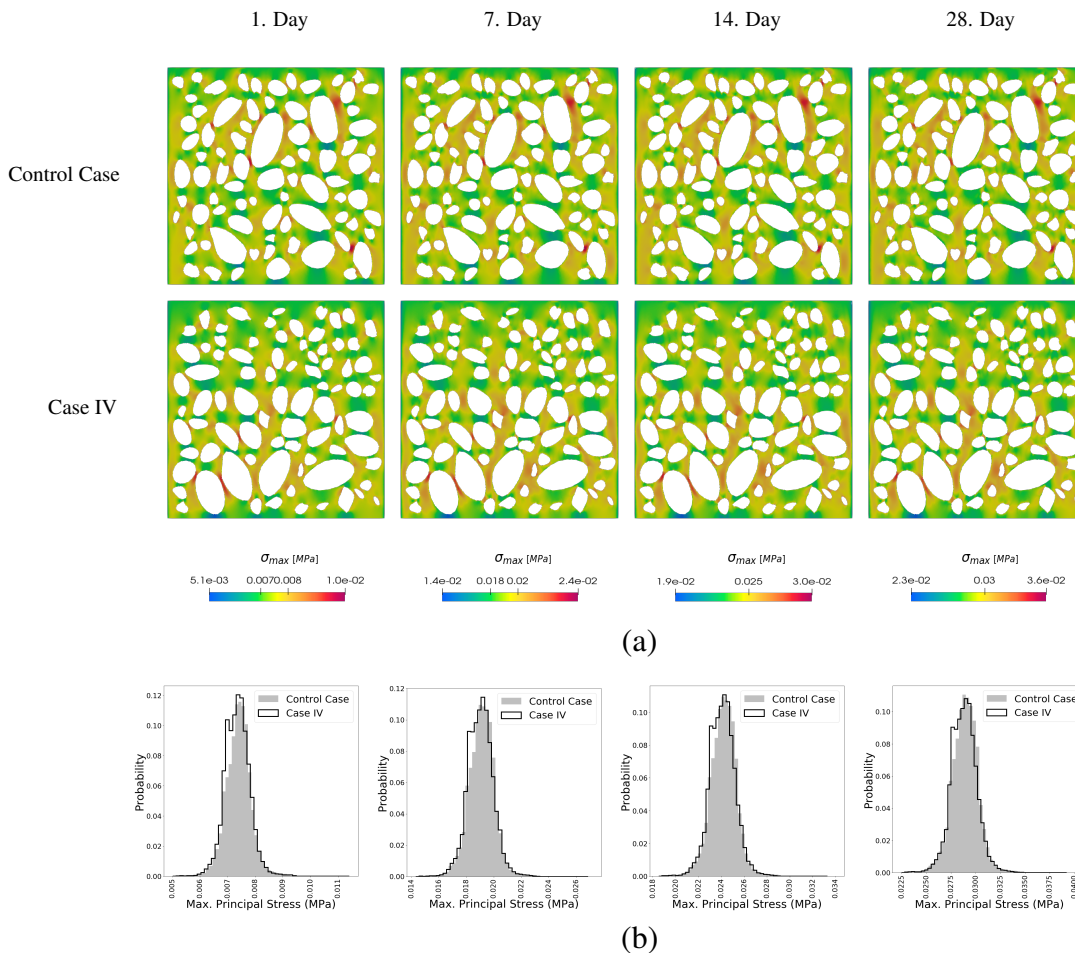


Figure 4.16: Maximum principal stress values (a) Contour plots (b) Histograms

Each row of the Figures 4.16(a) and 4.17(a) represents the case stated at the far left of the row and each column represents the end of the day from which the values are taken, for every column corresponding legend is given at the base of the column.

Generation of a segregated meso-structure forces the bigger aggregates to be placed at the bottom of the meso-structure and the probability of smaller aggregates to be placed at the top places of the meso-structure increases. Aggregates being close to each other results in stress concentrations. Although bigger aggregates cause stress concentration at the bottom of the meso-structure the smaller ones are going to be placed far away from each other at the top and this fact cause more mortar area to prevent having stress concentrations and it could be seen in Figure 4.16 Case IV has a higher probability of having smaller values of maximum principal stresses than the Control Case.

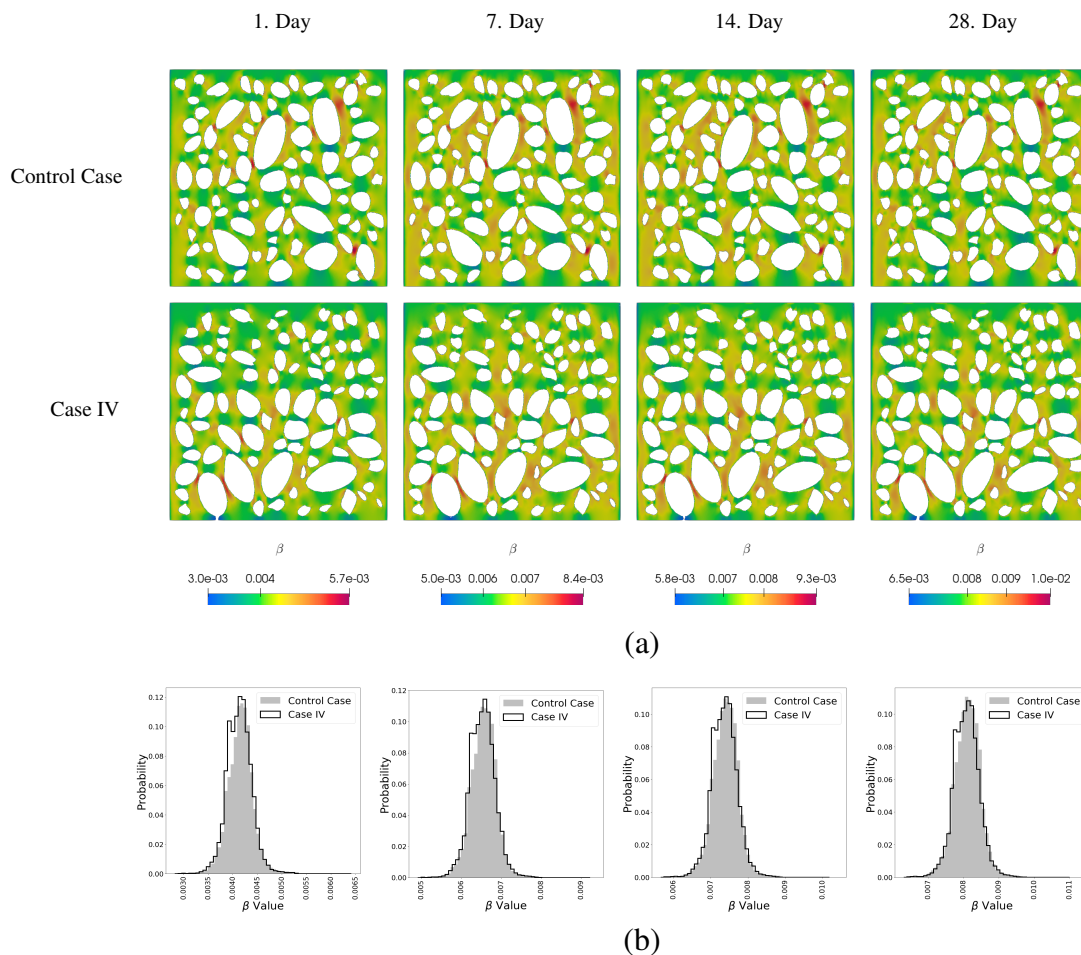


Figure 4.17: β values (a) Contour plots (b) Histograms

4.2.3 Elongation Ratio

Elongation ratio generally associated with different types of aggregate shapes. Crushed aggregates are generally flaky and elongated unlike coarse aggregates, which are generally round. Elongation ratio of Case V varies between 1 and 3. At the end of 28 days, the maximum principal stress obtained is 0.039 MPa and the maximum β ratio is 0.011. The principal stress and β values are shown for the compared cases in Figures 4.18(a) and 4.19(a). For every case the maximum principal stress and β values are shown for different days to be able to observe the evolutions of them. The days are selected to be 1, 7, 14, and 28. Each row of the Figures 4.18(a) and 4.19(a) represents the case stated at the far left of the row and each column represents the the end of the day from which the values are taken, for every column corresponding legend is given at the base of the column.

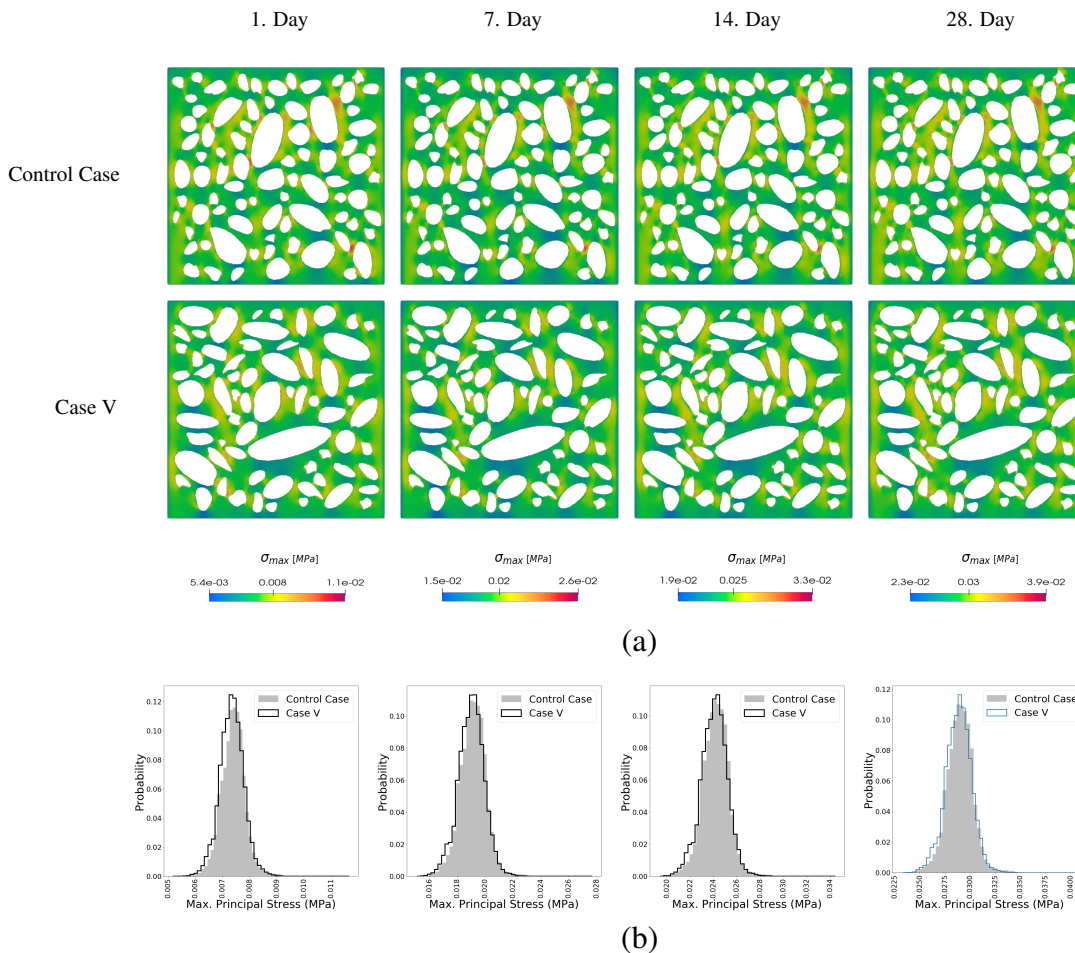


Figure 4.18: Maximum principal stress values (a) Contour plots (b) Histograms

Having a greater elongation ratio cause aggregates to have smooth edges and it is expected that Case V should has less stress concentration spots, in Figure 4.18 the validation of that Control Case has a higher probability of having higher values of maximum principal stresses due to having more stress concentrations can be done.

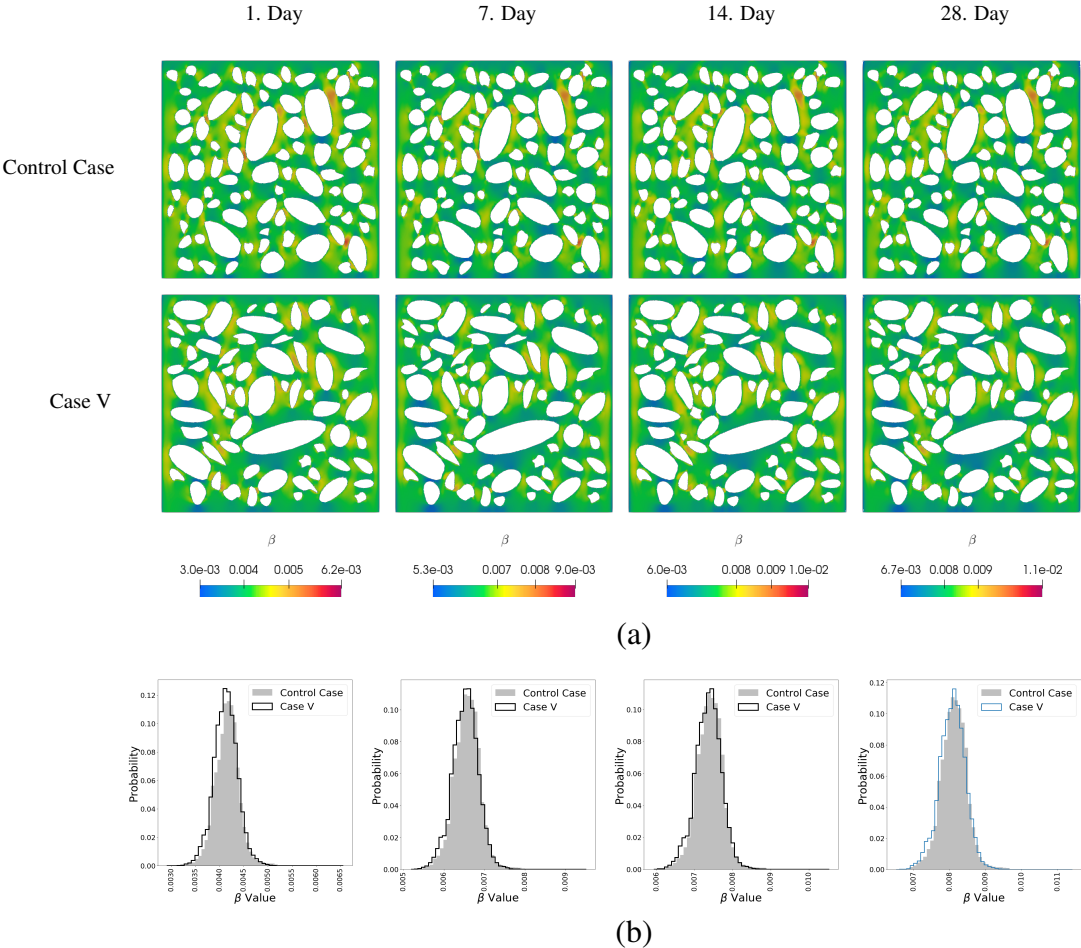


Figure 4.19: β values (a) Contour plots (b) Histograms

4.2.4 Shape

The investigation of effect of having sharp edges will be conducted in this section. For this purpose, two meso-structures, one having sharp corner aggregates and the other one having rounded corner aggregates considered. To evaluate only this effect, the meso-structure having sharp-corner aggregates is obtained then the cubic splines are fitted to nodes of each aggregate to be able to obtain the one having rounded-cornered aggregates. By doing that, two equivalent meso-structures are obtained.

Case VI, control case, has the maximum principal stress of 0.0035 MPa and β ratio of 0.0097 at the end of 28 days. Case VII has the maximum principal stress of 0.0034 MPa and β ratio of 0.009 at the end of 28 days. The principal stress and β values are shown for the compared cases in Figures 4.20(a) and 4.21(a). For every case the maximum principal stress and β values are shown for different days to be able to observe the evolutions of them. The days are selected to be 1, 7, 14, and 28. Each row of the Figures 4.20(a) and 4.21(a) represents the case stated at the far left of the row and each column represents the the end of the day from which the values are taken, for every column corresponding legend is given at the base of the column.

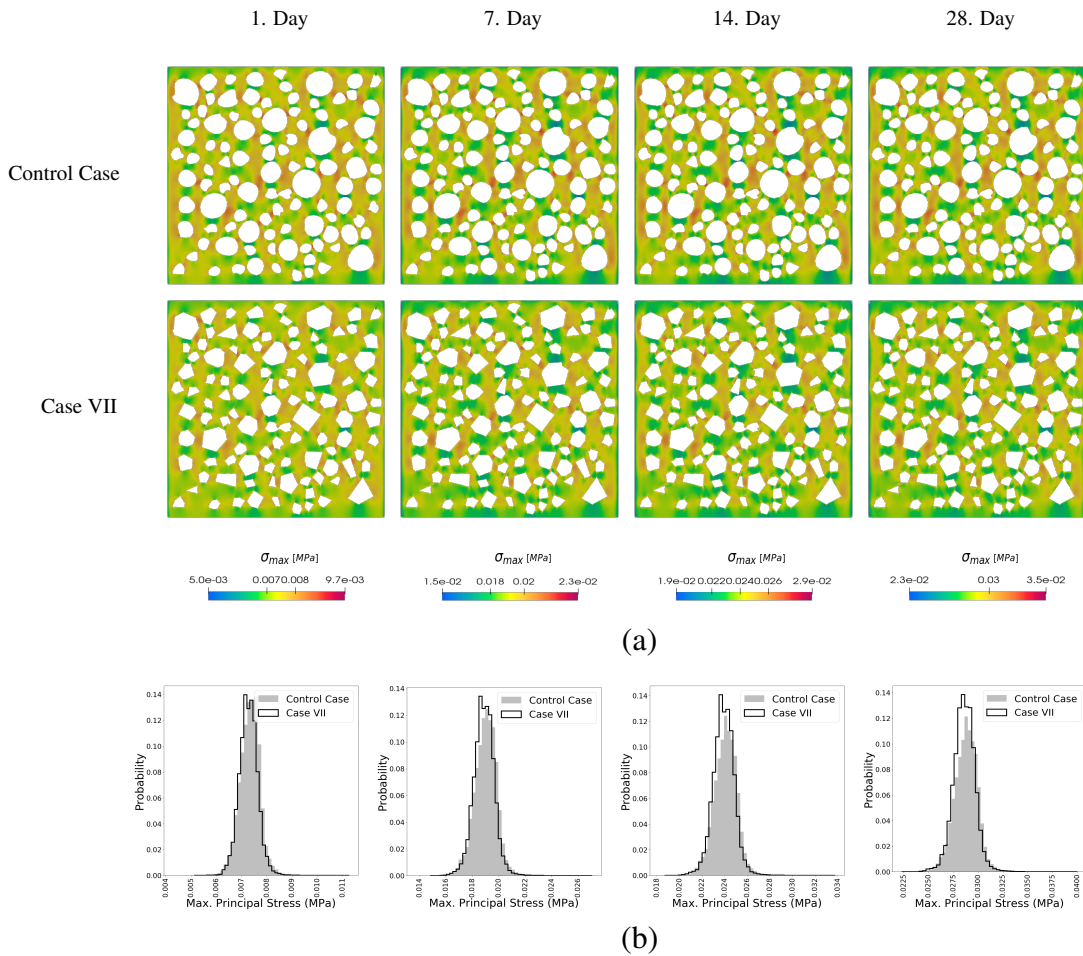


Figure 4.20: Maximum principal stress values (a) Contour plots (b) Histograms

Current comparison could not support the observation of stress concentrations around the sharp edges of aggregates. The reason behind that can be the autogenous shrinkage could not be large enough to highlight this fact. A meso-structure under me-

chanical or thermal loading could demonstrate this fact better. The rounded case, Control Case, have area ratio greater than the case with sharp edges, Case VII, so that the histogram plots show that in Control Case it is higher probability to have higher maximum principal stresses.

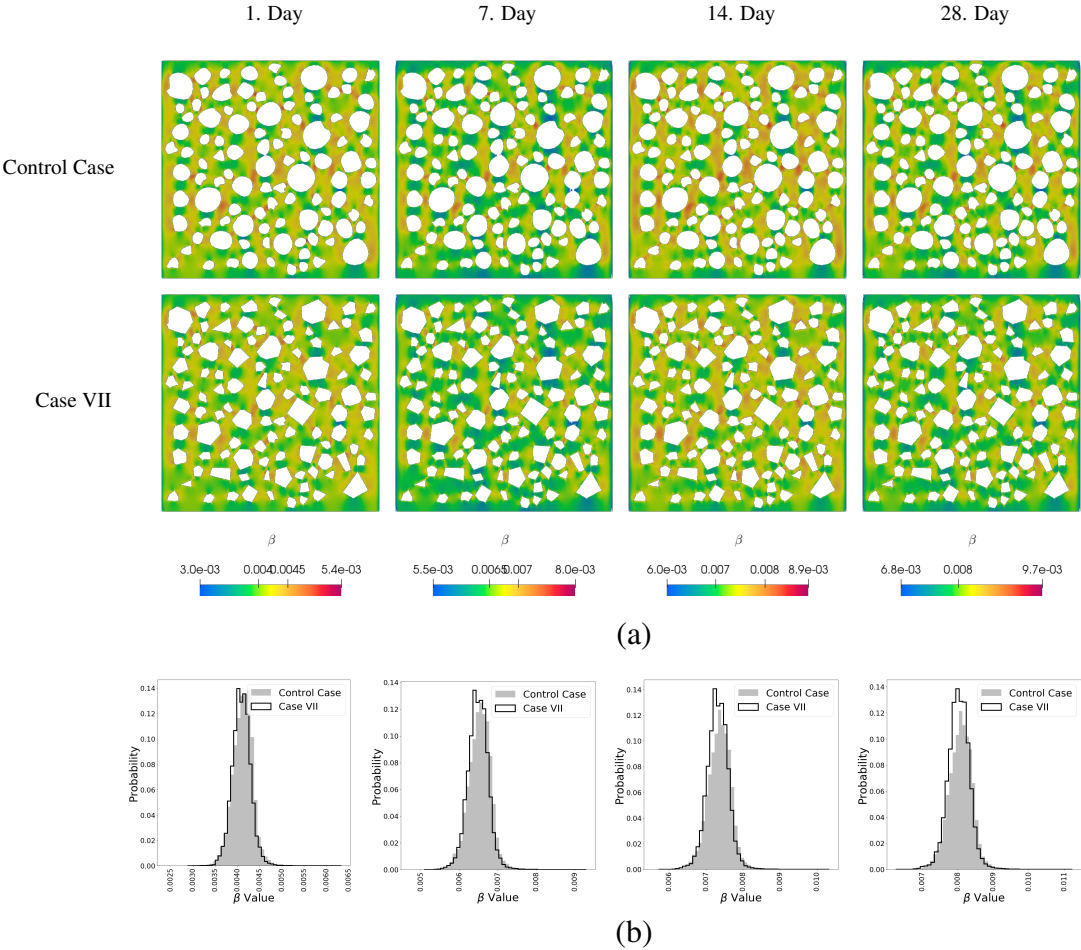


Figure 4.21: β values (a) Contour plots (b) Histograms

4.3 Fracture Behavior in Tension

In this section, a study on how the presence of residual stresses affect the behavior of hardened meso-structure and how different type of meso-structures affect their own behavior are conducted in Sections 4.3.1 and 4.3.2, respectively. The conducted analyses are aimed to represent two consequent processes which are the hardening and the tensile loading once it is hardened. The hardening process is already discussed

in Section 4.2 and the tensile loading is aimed to be discussed. The investigation of fracture behavior is done using brittle phase-field fracture model as it is described in Chapter 3. The presence of residual stresses is aimed to observe, that is why the cases given in Table 4.4 are analyzed with and without residual stresses. The translation in y direction of the nodes at bottom edge are fixed in y direction and the node placed at the left bottom edge is fixed also in x direction, the displacement is applied proportional to the time at $y = 150$ mm in y direction as it is shown in Figure 4.22. The evolution of the crack phase-field in the aggregates is suppressed through a high value of the critical energy that acts as a threshold value for crack initiation. The formation of crack in the Interfacial Transition Zone (ITZ) on the surface of an aggregate is modeled by means of zero-thickness cohesive zone elements that are placed between the aggregate and the mortar to represent the ITZ.

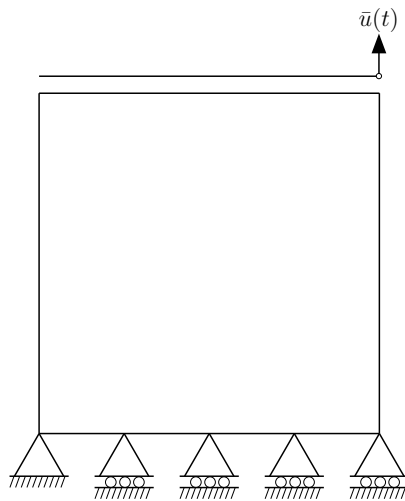


Figure 4.22: Boundary Conditions

Cohesive Zone Elements. The formation of cracks can be represented using cohesive zone elements which extends the crack while applying surface traction. In this work the implemented model of cohesive zone elements suggested by Corrado and Molinari [34].

The crack opening is represented by a vector Δ whose the tangential component is denoted by Δ_t and the normal component by Δ_n . The cohesive traction is expressed

as

$$\mathbf{T} = (\Delta_t \mathbf{t} + \Delta_n \mathbf{n})K \quad (4.4)$$

where \mathbf{T} consists of normal and tangential components T_n and T_t with respect to the crack surfaces. Moreover, the parameter K is the stiffness, \mathbf{t} and \mathbf{n} are tangent and normal vectors to the crack surface respectively. The stiffness depend on the effective crack opening displacement which is stated as

$$\delta = \sqrt{\Delta_t + \Delta_n}. \quad (4.5)$$

The loading and the unloading-reloading regime is decided according to the maximum effective opening displacement over time δ_{max} . The stiffness is indicated for $\delta = \delta_{max}$ as

$$K = \frac{\sigma_c}{\delta} \left(1 - \frac{\delta}{\delta_c}\right) \quad (4.6)$$

where σ_c is the tensile strength and δ_c is the critical opening displacement.

For the unloading-reloading path the stiffness is stated as

$$K = \frac{\sigma_c}{\delta_{max}} \left(1 - \frac{\delta_{max}}{\delta_c}\right) \quad (4.7)$$

The initial stiffness for $\delta_{max} < \delta_i$ is stated as

$$K = \frac{\sigma_c}{\delta_i}. \quad (4.8)$$

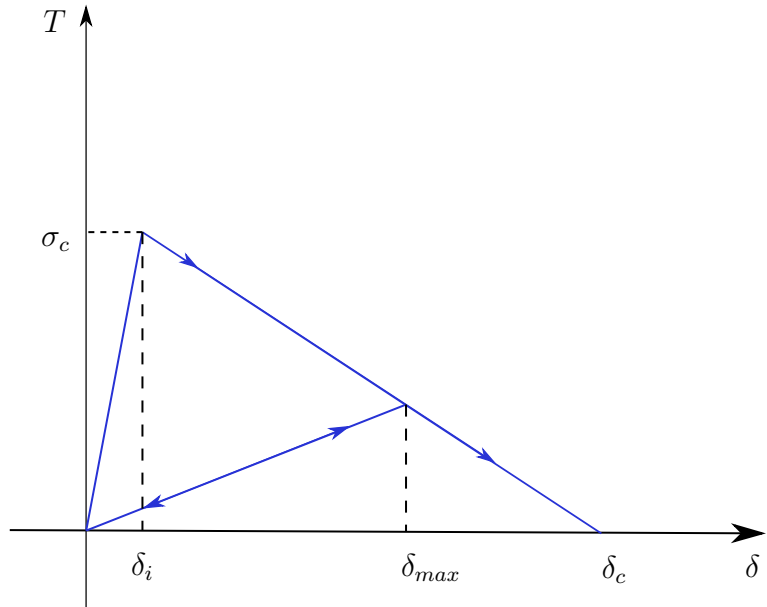


Figure 4.23: Unloading reloading path for cohesive zone element

The values of parameters that are related with the cohesive zone elements are given in Table 4.6.

Table 4.6: Cohesive Zone Element Parameters

σ_c	δ_i	δ_c
(N/mm)	(mm)	(mm)
1.3	4.6×10^{-4}	4.6×10^{-2}

The tangential traction is treated as a linear loading-unloading path, and due to the stability issues that it might create, the stiffness of it is taken small enough to neglect its effect.

4.3.1 Effect of Residual Stresses

The development of residual stresses through hardening of mortar results in micro-cracks. Micro-cracks builds up to macro-crack in hardened meso-structure under tensile loads. Cases given in Table 4.4 are examined under tensile loading in the presence and absence of the residual stresses. The load displacement curves; crack pattern with and without residual stresses for every case are given in Figures 4.24-4.30.

Case I (Control Case). The maximum loads obtained with and without the presence of residual stresses are 258 N and 266 N for control case under tensile loading respectively. Load displacement curve; crack patterns with and without the presence of residual stresses are shown in Figure 4.24. The presence of residual stresses cause the meso-structure to obtain a lower value of maximum load and it also decreases the stiffness of the meso-structure. Both effects can be observed in Figure 4.24(a). The presence of the residual stresses can result in the change of the crack pattern as it can be seen from Figures 4.24(b) and 4.24(c). Toughness values are calculated as 2.9 mJ and 3.4 mJ with and without the residual stresses, respectively. Furthermore, the toughness of the section with the residual stresses is slightly less than that of the same section in the absence of residual stresses.

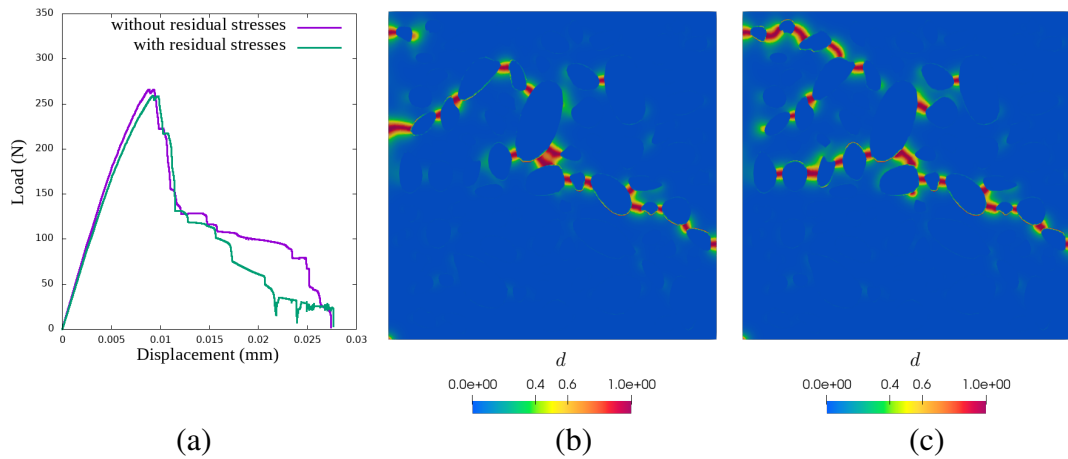


Figure 4.24: Control case: (a) Load displacement curve (b) Fracture formation with residual stresses (c) Fracture formation without residual stresses

Case II. The maximum loads obtained are 287 N and 297 N with and without the residual stresses, respectively. The decrease in initial stiffness and the decrease in attaining lower values of maximum load are observed in Figure 4.25(a). It can be observed from Figures 4.25(b) and 4.25(c) the crack pattern are very similar. This is also reflected by the similar toughness values, which are calculated as 2.8 mJ.

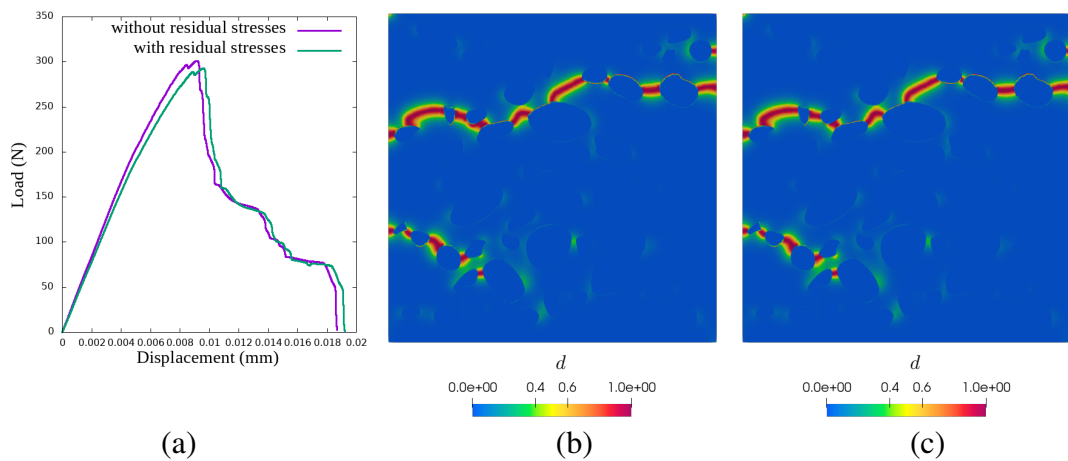


Figure 4.25: Case II: (a) Load displacement curve (b) Fracture formation with residual stresses (c) Fracture formation without residual stresses

Case III. The maximum loads obtained are 231 N and 236 N with and without the residual stresses, respectively. The decrease in initial stiffness and the decrease in attaining lower values of maximum load are observed in Figure 4.26(a). It can be observed from Figures 4.26(b) and 4.26(c) the crack pattern are very similar, so do the toughness values, which are calculated as 3.8 mJ.

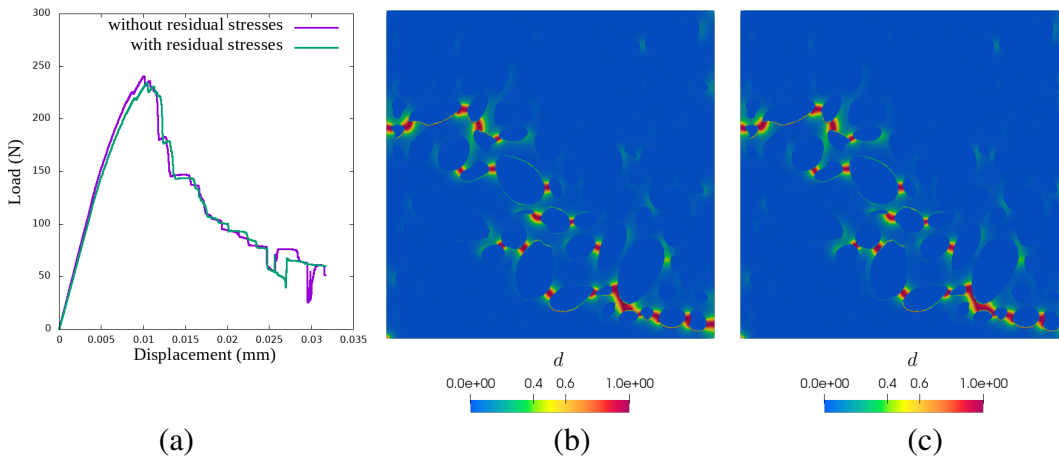


Figure 4.26: Case III: (a) Load displacement curve (b) Fracture formation with residual stresses (c) Fracture formation without residual stresses

Case IV. The maximum loads obtained are 254 N and 261 N with and without the residual stresses, respectively. The decrease in initial stiffness and the decrease in the attained values of maximum load are observed in Figure 4.27(a). It can be observed from Figures 4.27(b) and 4.27(c) the crack patterns are very similar, so do the toughness values, which are calculated as 2.5 mJ. Forcing bigger aggregate to be placed at the bottom of the meso-structure results in aggregates at these spots to become far close to each other. Therefore, at the bottom part of the meso-structure the stress concentration occurs so that the crack pattern is likely to be in the bottom part of the meso-structure.

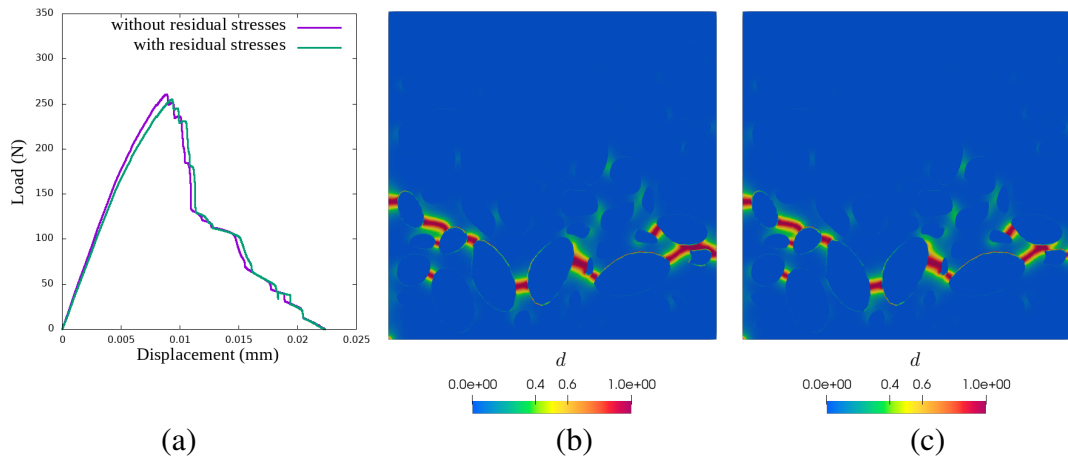


Figure 4.27: Case IV: (a) Load displacement curve (b) Fracture formation with residual stresses (c) Fracture formation without residual stresses

Case V. The maximum loads obtained are 242 N and 248 N with and without the residual stresses, respectively. The decrease in initial stiffness and the decrease in the attained values of the maximum load are observed in Figure 4.28(a). It can be observed from Figures 4.28(b) and 4.28(c) the crack patterns are very similar, so do the toughness values, which are calculated as 2.6 mJ.

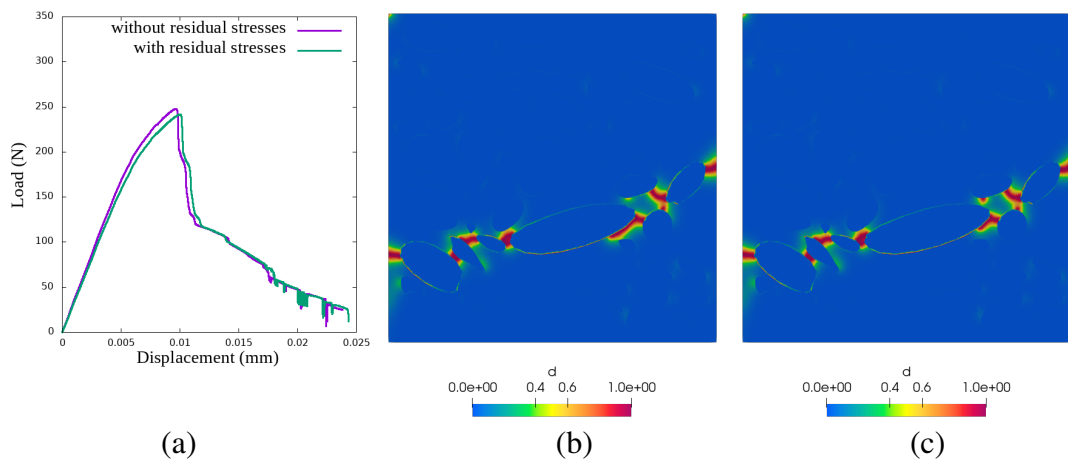


Figure 4.28: Case V: (a) Load displacement curve (b) Fracture formation with residual stresses (c) Fracture formation without residual stresses

Case VI (Control Case). The maximum loads obtained are 290 N and 298 N with and without the presence of residual stresses, respectively. The decrease in initial stiffness and the decrease in the attained values of the maximum load are observed in Figure 4.29(a). It can be observed from Figures 4.29(b) and 4.29(c) the crack patterns are very similar. However, there is a slight difference between toughness values which are calculated as 3 mJ and 2.7 mJ with and without the residual stresses, respectively.

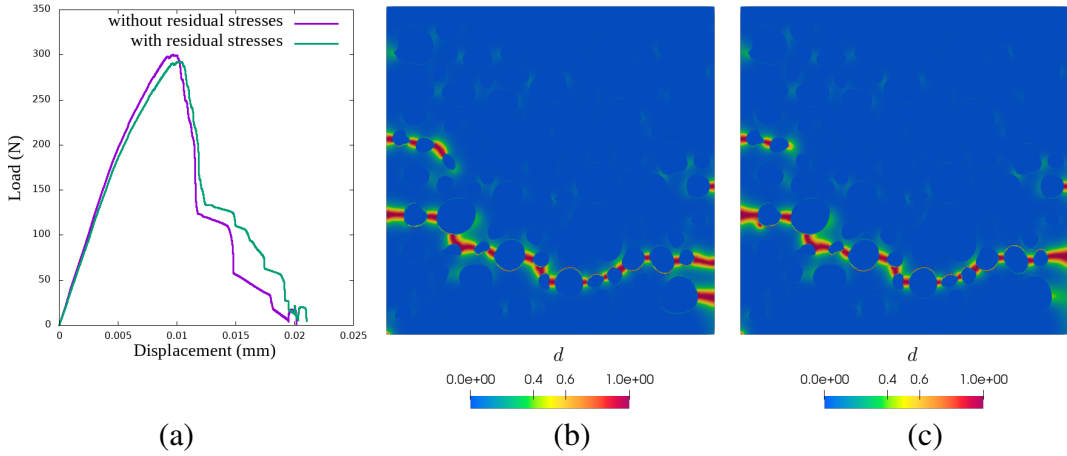


Figure 4.29: Case VI: (a) Load displacement curve (b) Fracture formation with residual stresses (c) Fracture formation without residual stresses

Case VII. The maximum loads obtained are 331 N and 341 N with and without the presence of residual stresses, respectively. The decrease in initial stiffness and the decrease in the attained values of the maximum load are observed in Figure 4.30(a). It can be observed from Figures 4.30(b) and 4.30(c) the crack patterns are very similar, so do the toughness values, which are calculated as 3.1 mJ.

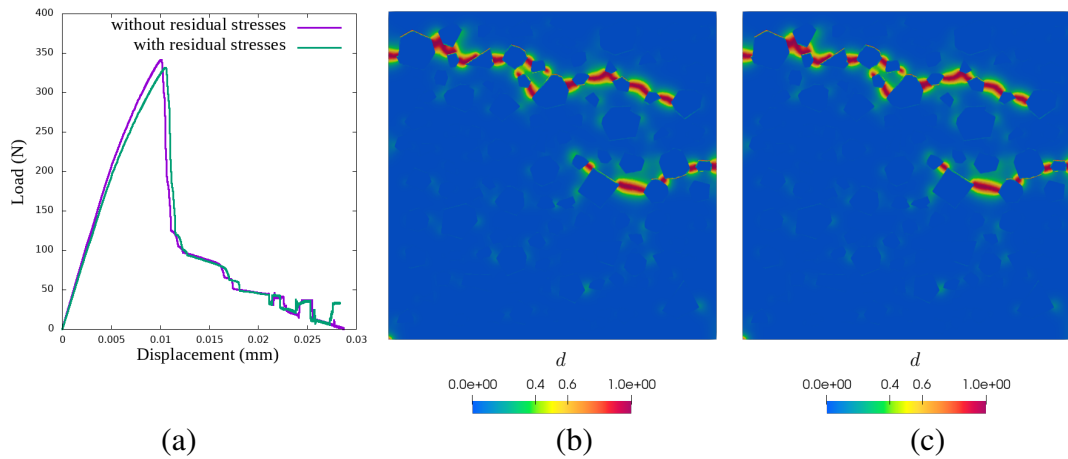


Figure 4.30: Case VII: (a) Load displacement curve (b) Fracture formation with residual stresses (c) Fracture formation without residual stresses

4.3.2 Comparison of Cases

The cases given in Table 4.4 are compared against Control Case under tensile loading using brittle phase-field model stated in Chapter 3. The comparison of the cases with and without the residual stresses shows the same behavior, and thus, only the results obtained without residual stresses will be presented.

Area Ratio. Case I (Control Case), Case II, and Case III are compared in order to observe the effect of the area ratio of aggregates. Having more aggregate increases the general stiffness of the meso-structure since aggregate is stiffer than the mortar. However, this fact could not be observed with the results. Figure 4.31 shows that Case II, where the area ratio is the smallest, is the stiffest one and it experiences the highest maximum load than the others while Case III, where the area ratio is the highest, is the least stiff one and it experiences the lowest maximum load than the others. The reason behind this fact is thought to be cohesive zone elements add compliance to the meso-structure. The contribution of aggregate stiffness to the general stiffness of the meso-structure could not be added up due to cohesive zone elements. Increase in the area ratio of aggregates causes the total perimeter of aggregates to increase and that causes the total number of cohesive zone elements to increase and more compliance

is added to the system. The total perimeter of aggregates are calculated as 2827 mm, 1927 mm, and 3476 mm for Case I, Case II, and Case III, respectively. Analyses without cohesive zone elements are conducted to observe the compliance added by the cohesive zone elements. It is observed that the load displacement curves become similar for Case I, Case II, and Case III. However, it should be noted that the crack patterns obtained with these analyses differ from those conducted with cohesive zone elements.

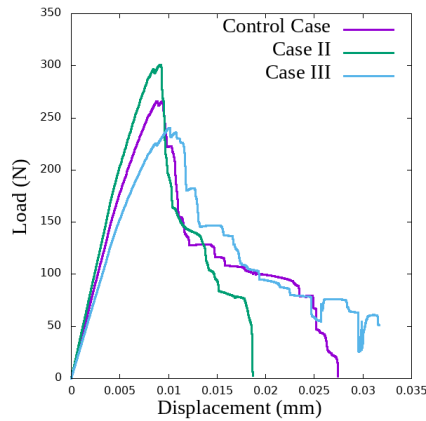


Figure 4.31: Load displacement curve for area ratio comparison

Segregation. The values of parameters generated for Case IV is the same with Control Case. Therefore, both of them should attain close values of maximum loads and close values of stiffnesses. This fact can be seen in Figure 4.32.

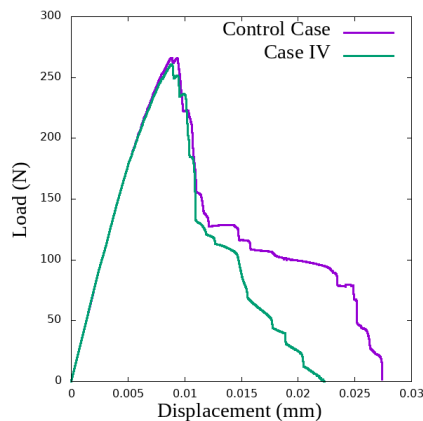


Figure 4.32: Load displacement curve for segregation comparison

Elongation Ratio. Control Case and Case V are aimed to be examine the effect of elongation ratio of aggregates. Load displacement curves are given in Figure 4.33. Case I experienced a higher value of maximum load, and although the initial stiffnesses of both cases are the same, the stiffness of Case V started to decrease as the applied load approached its maximum. Having greater elongation ratio cause aggregates to have round edges, so that it is expected to Control Case to have more stress concentrations than Case V; therefore, the behavior seen in Figure 4.33 should be opposite of that. However, although there is no supplied proof of that, having greater elongation ratio could cause aggregates to be placed closer to each other, thus, more stress concentration could occur in Case V and the behavior in Figure 4.33. Therefore, without additional evidence, it is difficult to determine the exact behavior seen in Figure 4.33.

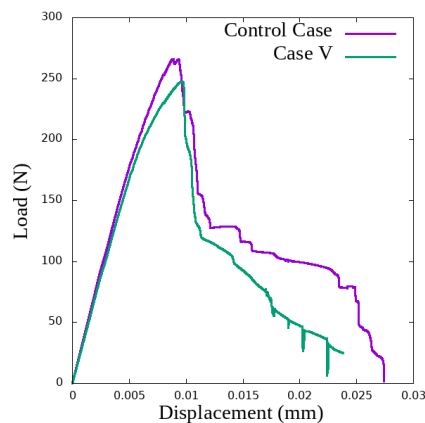


Figure 4.33: Load displacement curve for elongation ratio comparison

Shape. The comparison regarding for the effect of aggregate shape is done with Case VI (Control Case) and Case VII which are equivalent meso-structures of each other. Load displacement curves are given in Figure 4.34. Having sharp corners results in more stress concentrations to occur and those occurrences leads to fracture to initiate. However, the total perimeters of aggregates are calculated as 3044 mm and 2900 mm for Case VI and Case VII, respectively. Therefore, the total number of cohesive elements are greater in Case VI. Thus, the compliance that is added up to the system by the cohesive zone elements is observed.

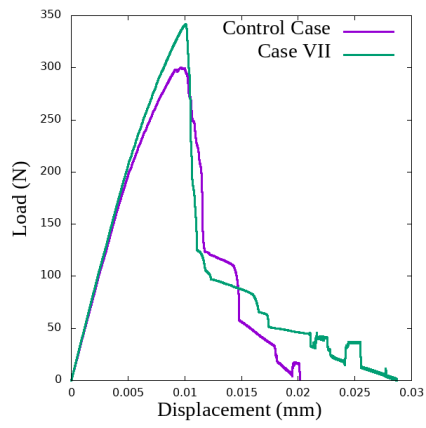


Figure 4.34: Load displacement curve for shape comparison

CHAPTER 5

CONCLUDING REMARKS

In this thesis, the evolution of residual stresses due to autogenous shrinkage of hardening mortar at mesoscale has been examined. For this purpose, seven different meso-structures of concrete that differ from one another by different geometrical, fractional, and topological features have been generated. The fracture behavior of these sections of concrete with distinct meso-structures have then been analyzed under direct tension using the brittle phase-field model based on the work of Miehe et al. [44] and the cohesive zone elements based on the work of Corrado and Molinari [34] in the presence and absence of residual stresses. The meso-structures examined in this study have been generated using the Take-and-Place method, suggested in Wang et al. [22]. The hydration kinetics that characterizes the shrinkage and aging mechanism has been adopted from the work of Cervera et al. [46]. Shrinkage strain is applied as being a linear function of the degree of hydration.

The development of principal stresses and the ratio of the maximum principal stresses to the instantaneous tensile strengths are used as the measures used in the comparison of seven different meso-structures. These different cases have been used to investigate the effects of the area ratio, the segregation, the elongation ratio, and the sharpness of coarse aggregates. The contour and histogram plots of principal stresses and the β values have been used to compare the cases. It is observed that a greater area ratio of aggregates increases the probability of having higher values of principal stresses, segregation increases the probability of smaller values of principal stresses and the occurrence of stress concentration exists on the locations where bigger aggregates are accumulated. However, it is worth noting that the autogenous shrinkage may not be enough to highlight the fact of sharp edges of aggregates leading to stress concentrations. The distinction of contour plots of principal stresses and their histogram plots

has not been come out to be pronounced for the compared cases and also the stress concentrations around the sharp edges of aggregates has not been observed due to residual stress development. These are due probably to the relatively low levels of autogenous shrinkage and its uniform distribution throughout the mortar. It is seen that the presence of residual stresses both decrease the stiffness of the meso-structure and reduce the value of maximum load that could be attained. The comparison of fracture behavior of different cases validates the stress concentrations occur between aggregates that are close to each other and results in the formation of crack. The cases where segregation is observed clearly show that the crack formation occur at lower parts of the meso-structure where the bigger aggregates are accumulated. However, the cohesive zone elements add to the compliance of the meso-structures as clearly observed in the comparison where a higher area ratio resulted in a decreased in stiffness and the ultimate load. Also, similar load displacement curves are obtained with analyses conducted without cohesive zone elements for different cases. Therefore, validation of compliance can be done. However, it should be noted that the crack patterns obtained with these analyses differ from those conducted with cohesive zone elements. Furthermore, the formation of crack due to stress concentrations around sharp edges of aggregates has been observed due to the compliance related with cohesive zone elements. Overall, based on the results obtained it can be stated that while the pre-cracking stiffness and the tensile strength of meso-structures are primarily controlled by the properties of cohesive elements used to model ITZ, the toughness of the sections is chiefly governed by the pattern of cracking in mortar that is essentially regulated by the stress localizations due to shrinkage and the properties of coarse aggregates.

As it is the case for the failure behavior of any composite material, the cohesive behavior of interfacial zone governs the overall macroscopic behavior a meso-structure. Therefore, besides the correct account for the residual stress evolution, the sound modeling of ITZ is of key importance as clearly demonstrated through the examples presented in this study. Therefore, a precise parameter study should be conducted on cohesive zone elements to suppress the spurious introduction of compliance to the meso-structure. Moreover, future studies could include different types of shrinkage for more accurate representation of the development of residual stresses. Including different types of shrinkage may result in a more clear comparison between different

cases.

REFERENCES

- [1] D. Bentz, M. Geiker, and K. Hansen, “Shrinkage-reducing admixtures and early-age desiccation in cement pastes and mortars,” *Cement and Concrete Research*, vol. 31, no. 7, pp. 1075–1085, 2001.
- [2] D. P. Bentz, G. Sant, and J. Weiss, “Early-age properties of cement-based materials. i: Influence of cement fineness,” *Journal of Materials in Civil Engineering*, vol. 20, no. 7, pp. 502–508, 2008.
- [3] A. Loukili, D. Chopin, A. Khelidj, and J.-Y. Le Touzo, “A new approach to determine autogenous shrinkage of mortar at an early age considering temperature history,” *Cement and Concrete Research*, vol. 30, no. 6, pp. 915–922, 2000.
- [4] T. Lu, Z. Li, and H. Huang, “Restraining effect of aggregates on autogenous shrinkage in cement mortar and concrete,” *Construction and Building Materials*, vol. 289, p. 123166, 2021.
- [5] P. Taylor, T. V. Dam, L. Sutter, and G. Fick, *Integrated materials and construction practices for concrete pavement: A state-of-the-practice manual*. Federal Highway Administration. Office of Pavement Technology, United States, 2007.
- [6] D. Gawin, F. Pesavento, and B. A. Schrefler, “Hygro-thermo-chemo-mechanical modelling of concrete at early ages and beyond. part i: hydration and hygro-thermal phenomena,” *International Journal for Numerical Methods in Engineering*, vol. 67, no. 3, pp. 299–331, 2006.
- [7] D. Gawin, F. Pesavento, and B. A. Schrefler, “Hygro-thermo-chemo-mechanical modelling of concrete at early ages and beyond. part ii: shrinkage and creep of concrete,” *International Journal for Numerical Methods in Engineering*, vol. 67, no. 3, pp. 332–363, 2006.
- [8] G. Di Luzio and G. Cusatis, “Hygro-thermo-chemical modeling of high perfor-

- mance concrete. i: Theory,” *Cement and Concrete Composites*, vol. 31, no. 5, pp. 301–308, 2009.
- [9] G. Di Luzio and G. Cusatis, “Hygro-thermo-chemical modeling of high-performance concrete. ii: Numerical implementation, calibration, and validation,” *Cement and Concrete Composites*, vol. 31, no. 5, pp. 309–324, 2009.
- [10] M. Bouasker, P. Mounanga, P. Turcry, A. Loukili, and A. Khelidj, “Chemical shrinkage of cement pastes and mortars at very early age: Effect of limestone filler and granular inclusions,” *Cement and Concrete Composites*, vol. 30, no. 1, pp. 13–22, 2008.
- [11] J. Zhang, E. A. Weissinger, S. Peethamparan, and G. W. Scherer, “Early hydration and setting of oil well cement,” *Cement and Concrete Research*, vol. 40, no. 7, pp. 1023–1033, 2010.
- [12] O. M. Jensen and P. F. Hansen, “Autogenous deformation and rh-change in perspective,” *Cement and Concrete Research*, vol. 31, no. 12, pp. 1859–1865, 2001.
- [13] P. Grassl, H. S. Wong, and N. R. Buenfeld, “Influence of aggregate size and volume fraction on shrinkage induced micro-cracking of concrete and mortar,” *Cement and Concrete Research*, vol. 40, no. 1, pp. 85–93, 2010.
- [14] M. C. Garci Juenger and H. M. Jennings, “Examining the relationship between the microstructure of calcium silicate hydrate and drying shrinkage of cement pastes,” *Cement and Concrete Research*, vol. 32, no. 2, pp. 289–296, 2002.
- [15] A. R. Gangolu, “Long-term drying shrinkage of mortar- influence of silica fume and size of fine aggregate,” *Cement and Concrete Research*, vol. 31, pp. 171–175, 02 2001.
- [16] I. Yurtdas, N. Burlion, and F. Skoczylas, “Triaxial mechanical behaviour of mortar: Effects of drying,” *Cement and Concrete Research*, vol. 34, no. 7, pp. 1131–1143, 2004.
- [17] E. Boghossian and L. D. Wegner, “Use of flax fibres to reduce plastic shrinkage cracking in concrete,” *Cement and Concrete Composites*, vol. 30, no. 10, pp. 929–937, 2008.

- [18] K. Yang, M. Zhong, B. Magee, C. Yang, C. Wang, X. Zhu, and Z. Zhang, "Investigation of effects of portland cement fineness and alkali content on concrete plastic shrinkage cracking," *Construction and Building Materials*, vol. 144, pp. 279–290, 2017.
- [19] A. Almusallam, M. Maslehuddin, M. Abdul-Waris, and M. Khan, "Effect of mix proportions on plastic shrinkage cracking of concrete in hot environments," *Construction and Building Materials*, vol. 12, no. 6, pp. 353–358, 1998.
- [20] S. Fu, T. He, G. Wang, S. Zhang, L. Zou, and S. Chen, "Evaluation of cracking potential for concrete arch dam based on simulation feedback analysis," *Science China Technological Sciences*, vol. 54, p. 565-572, 2011.
- [21] W. Ren, Z. Yang, R. Sharma, C. Zhang, and P. J. Withers, "Two-dimensional x-ray ct image based meso-scale fracture modelling of concrete," *Engineering Fracture Mechanics*, vol. 133, pp. 24–39, 2015.
- [22] Z. Wang, A. Kwan, and H. Chan, "Mesoscopic study of concrete i: generation of random aggregate structure and finite element mesh," *Computers & Structures*, vol. 70, no. 5, pp. 533–544, 1999.
- [23] L. Liu, D. Shen, H. Chen, and W. Xu, "Aggregate shape effect on the diffusivity of mortar: A 3d numerical investigation by random packing models of ellipsoidal particles and of convex polyhedral particles," *Computers & Structures*, vol. 144, pp. 40–51, 2014.
- [24] X. Wang, Z. Yang, J. Yates, A. Jivkov, and C. Zhang, "Monte carlo simulations of mesoscale fracture modelling of concrete with random aggregates and pores," *Construction and Building Materials*, vol. 75, pp. 35–45, 2015.
- [25] H. Ma, W. Xu, and Y. Li, "Random aggregate model for mesoscopic structures and mechanical analysis of fully-graded concrete," *Computers & Structures*, vol. 177, pp. 103–113, 2016.
- [26] P. Grassl and R. Rempling, "A damage-plasticity interface approach to the meso-scale modelling of concrete subjected to cyclic compressive loading," *Engineering Fracture Mechanics*, vol. 75, no. 16, pp. 4804–4818, 2008.

- [27] S.-M. Kim and R. K. Abu Al-Rub, "Meso-scale computational modeling of the plastic-damage response of cementitious composites," *Cement and Concrete Research*, vol. 41, no. 3, pp. 339–358, 2011.
- [28] Y. Huang, Z. Yang, W. Ren, G. Liu, and C. Zhang, "3d meso-scale fracture modelling and validation of concrete based on in-situ x-ray computed tomography images using damage plasticity model," *International Journal of Solids and Structures*, vol. 67-68, pp. 340–352, 2015.
- [29] O. Yilmaz and J.-F. Molinari, "A mesoscale fracture model for concrete," *Cement and Concrete Research*, vol. 97, pp. 84–94, 2017.
- [30] Q. Xiong, X. Wang, and A. P. Jivkov, "A 3d multi-phase meso-scale model for modelling coupling of damage and transport properties in concrete," *Cement and Concrete Composites*, vol. 109, p. 103545, 2020.
- [31] T. Nguyen, J. Yvonnet, Q.-Z. Zhu, M. Bornert, and C. Chateau, "A phase field method to simulate crack nucleation and propagation in strongly heterogeneous materials from direct imaging of their microstructure," *Engineering Fracture Mechanics*, vol. 139, pp. 18–39, 2015.
- [32] T. Nguyen, J. Yvonnet, Q.-Z. Zhu, M. Bornert, and C. Chateau, "A phase-field method for computational modeling of interfacial damage interacting with crack propagation in realistic microstructures obtained by microtomography," *Computer Methods in Applied Mechanics and Engineering*, vol. 312, pp. 567–595, 2016. Phase Field Approaches to Fracture.
- [33] Z.-J. Yang, B.-B. Li, and J.-Y. Wu, "X-ray computed tomography images based phase-field modeling of mesoscopic failure in concrete," *Engineering Fracture Mechanics*, vol. 208, pp. 151–170, 2019.
- [34] M. Corrado and J.-F. Molinari, "Effects of residual stresses on the tensile fatigue behavior of concrete," *Cement and Concrete Research*, vol. 89, pp. 206–219, 2016.
- [35] Y. Xu, Q. Xu, S. Chen, and X. Li, "Self-restraint thermal stress in early-age concrete samples and its evaluation," *Construction and Building Materials*, vol. 134, pp. 104–115, 2017.

- [36] T.-T. Nguyen, D. Waldmann, and T. Q. Bui, “Phase field simulation of early-age fracture in cement-based materials,” *International Journal of Solids and Structures*, vol. 191-192, pp. 157–172, 2020.
- [37] Y. Li, X. Ruan, Y. Yi, and L. Xu, “Multiphysics simulation for concrete early-age hydration behavior with mesoscopic modelling,” *Construction and Building Materials*, vol. 362, p. 129780, 2023.
- [38] M. Matallah, A. Taibi, T. Chimoto, and F. Maradzika, “Mesoscale investigation of mass concrete temperature control systems and their consequences on concrete mechanical behaviour,” *Frattura ed Integrità Strutturale*, vol. 16, pp. 416–437, 2022.
- [39] W. Qiu, S. FU, J. hua Zhu, C. Zeng, and J. Ye, “Meso-scale modelling of the thermo-mechanical response for concrete with complex-shaped aggregates in early age,” *Construction and Building Materials*, vol. 323, p. 126485, 2022.
- [40] W. Qiu, T. Ueda, S. Fu, Y. Han, J. Wang, and J. Ye, “Meso-scale computational modeling of the fracture of concrete with complex shaped aggregates under the self-restraint stress,” *Composite Structures*, vol. 303, p. 116267, 2023.
- [41] W. B. Fuller and S. E. Thompson, “The laws of proportioning concrete,” *Transactions of the American Society of Civil Engineers*, pp. 67–143, 1906.
- [42] G. Di Luzio and G. Cusatis, “Solidification–microprestress–microplane (smm) theory for concrete at early age: Theory, validation and application,” *International Journal of Solids and Structures*, vol. 50, no. 6, pp. 957–975, 2013.
- [43] M. Ambati, T. Gerasimov, and L. De Lorenzis, “A review on phase-field models of brittle fracture and a new fast hybrid formulation,” *Computational Mechanics*, vol. 55, no. 2, p. 383 – 405, 2015.
- [44] C. Miehe, L.-M. Schänzel, and H. Ulmer, “Phase field modeling of fracture in multi-physics problems. part i. balance of crack surface and failure criteria for brittle crack propagation in thermo-elastic solids,” *Computer Methods in Applied Mechanics and Engineering*, vol. 294, pp. 449–485, 2015.

- [45] F.-J. Ulm and O. Coussy, “Modeling of thermochemomechanical couplings of concrete at early ages,” *Journal of Engineering Mechanics*, vol. 121, no. 7, pp. 785–794, 1995.
- [46] M. Cervera, J. Oliver, and T. Prato, “Simulation of construction of rcc dams. i: Temperature and aging,” *Journal of Structural Engineering*, vol. 126, no. 9, pp. 1053–1061, 2000.
- [47] R. L. Taylor, “FEAP - finite element analysis program,” University of California, Berkeley, 2014.
- [48] S. Hert and M. Seel, “2D convex hulls and delaunay triangulations,” in *CGAL User and Reference Manual*, CGAL Editorial Board, 5.5.1 ed., 2022.